Journal of Materials Chemistry A

Accepted Manuscript

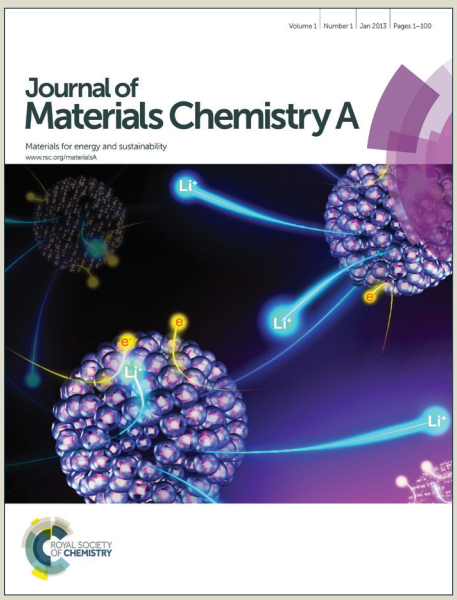

ROYAL SOCIETY OF CHEMISTRY

www.rsc.org/materialsA

Oxygen Surface Exchange Kinetics and Stability of $(La,Sr)_2CoO_{4\pm\delta}/La_{1-x}Sr_xMO_{3-\delta}$ (M = Co and Fe) Hetero-interfaces at Intermediate Temperatures

Dongkyu Lee[1,2,+], Yueh-Lin Lee[1,2,+], Wesley T. Hong[1,3], Michael D. Biegalski[4], Dane Morgan[5,*], and Yang Shao-Horn[1,2,3,*]

[1]Electrochemical Energy Laboratory, [2]Department of Mechanical Engineering, and [3]Department of Materials Science and Engineering, Massachusetts Institute of Technology, 77 Massachusetts Avenue, Cambridge, Massachusetts 02139, United States

[4]Center for Nanophase Materials Sciences, Oak Ridge National Laboratory, Oak Ridge, Tennessee 37831, United States

[5]Department of Materials Science and Engineering, University of Wisconsin–Madison, 1509 University Avenue, Madison, Wisconsin 53706, United States

Abstract

Heterostructured oxide interfaces created by decorating Ruddlesden-Popper (RP) phases on ABO_3 perovskites have shown not only pronounced cation segregation at the interface and in the RP phase but also enhanced kinetics for oxygen electrocatalysis at elevated temperatures. In this study, combining experimental and theoretical approaches, we report and compare the time-dependent surface exchange kinetics and stability of $(La_{0.5}Sr_{0.5})_2CoO_{4\pm\delta}$ (LSC_{214})-decorated $La_{0.6}Sr_{0.4}Co_{0.2}Fe_{0.8}O_{3-\delta}$ ($LSCF_{113}$) and $La_{0.8}Sr_{0.2}CoO_{3-\delta}$ (LSC_{113}) thin films. While LSC_{214} decoration on LSC_{113} greatly reduced the degradation in the surface exchange kinetics as a function of time relative to undecorated LSC_{113}, $LSCF_{113}$ with LSC_{214} coverage showed comparable surface exchange kinetics and stability relative to undecorated $LSCF_{113}$. This difference is attributed to stabilization of LSC_{113} surface by LSC_{214} decoration and greater stability of $LSCF_{113}$ against decomposition into secondary phases than LSC_{113}. This hypothesis is supported by density functional theory (DFT) computation, revealing greater surface Sr segregation for $LSCF_{113}$, which is predicted to have an SrO termination, than LSC_{113}, which is predicted to have a less Sr enriched $(La_{0.25}Sr_{0.75})O$ termination. Furthermore, DFT also showed a lower energy gain to move Sr from $LSCF_{113}$ into LSC_{214} relative to the LSC_{214}-LSC_{113} surface, and predicted the stability of $LSCF_{113}$, LSC_{113}, and LSC_{214} with 100% Sr substitution in their top (001) surface. The stability differences of Sr substitution (with La) in $LSCF_{113}$, LSC_{113}, and LSC_{214}, along with the assessed DFT decomposition free energies of fully Sr substituted $LSCF_{113}$, LSC_{113}, and LSC_{214}, correlate with experimental observation of surface stability trends in surface particle formation of $LSCF_{113}$ and LSC_{113} without and with LSC_{214} decoration.

Keywords

fuel cells, heterostructure interface, oxygen surface exchange kinetics, long-term stability, surface chemistry, cation interdiffusion, surface stability, density functional theory

1. Introduction

The majority of efficiency loss in lower-temperature solid oxide fuel cells (SOFCs) results from slow oxygen reduction reaction (ORR) kinetics at the cathode.[1-3] Lanthanum strontium manganite (LSM)[4-8] alloys are currently utilized as a cathode material and operate efficiently only at high temperatures such as 1000 °C. Therefore, there is a need to search for electrode materials with high catalytic activity, particularly for intermediate temperatures (500 – 700 °C) SOFCs. Mixed ionic and electronic conductors (MIECs) such as $La_{1-x}Sr_xCoO_{3-\delta}$ (LSC)[9-15] and $La_{1-x}Sr_xCo_{1-y}F_yO_{3-\delta}$ (LSCF)[16-20] perovskite oxides have been studied widely to promote the oxygen surface exchange kinetics at intermediate temperatures.

Oxide heterostructured interfaces such as the combination of a $(La_{0.5}Sr_{0.5})_2CoO_{4\pm\delta}$ (LSC_{214}) Ruddlesden-Popper (RP) and a LSC perovskite, which can exhibit remarkably high oxygen surface exchange kinetics, have been studied intensively.[21-33] Sase et al.[30] have reported ~3 orders of magnitude higher oxygen surface exchange coefficient (k^*) at the interfacial region between polycrystalline $La_{0.6}Sr_{0.4}CoO_{3-\delta}$ and LSC_{214} compared to their bulk values. This enhancement has been translated to a porous composite cathode having ~1 order of magnitude enhancement in activity reported by Yashiro et al.[33] In addition, pronounced enhancement in the surface exchange kinetics up to ~2 orders of magnitude[22] has been reported by decorating epitaxially grown LSC_{214} on (001)-oriented $La_{0.8}Sr_{0.2}CoO_{3-\delta}$ (LSC_{113}). Recent experimental and density functional theory (DFT) studies have suggested that the enhancement can be attributed to surface segregation of Sr in the perovksite structure at the LSC_{214}-LSC_{113} interface and surface segregation of Sr on the LSC_{214} surface.[23-26]

In this work, we focus on the influence of LSC_{214} surface decoration on the oxygen surface exchange kinetics and the time-dependent surface stability of epitaxial

$La_{0.6}Sr_{0.4}Co_{0.2}Fe_{0.8}O_{3-\delta}$ ($LSCF_{113}$) thin films, which is compared with an LSC_{214}-decorated LSC_{113} thin film. Therefore, in this study, we address if and how LSC_{214} decoration on the $LSCF_{113}$ surface can lead to any enhancement of the surface exchange kinetics and surface stability using epitaxial thin films as a model system. As part of this study, we provide DFT predictions of surface stability and composition (La/Sr and Co/Fe segregation) for LSC_{113} and $LSCF_{113}$ (001) surfaces. We find that the LSC_{214} decoration can enhance the oxygen surface exchange coefficient (k^q) of the $LSCF_{113}$ thin film only ~2 times in contrast to the pronounced enhancement in the k^q by ~2 orders of magnitude observed for the LSC_{113} thin film found in this study and previous work.[22, 34] We report that the LSC_{214}-decorated LSC_{113} exhibits much reduced degradation in k^q relative to LSC_{113} while LSC_{214}-decorated $LSCF_{113}$ and $LSCF_{113}$ show comparable loss in the surface exchange kinetics over time. Combined Auger electron spectroscopy (AES) and DFT studies suggest that reduced degradation associated with LSC_{214} decoration of LSC_{113} over time and the lack of changes associated with LSC_{214} decoration of $LSCF_{113}$ can be attributed to stabilization of LSC_{113} surface by LSC_{214} decoration and greater stability of $LSCF_{113}$ against decomposition into secondary phases than LSC_{113}.

2. Experimental Methods

2.1 Film deposition

Pulsed laser deposition (PLD) was utilized to deposit the (001)-oriented epitaxial $LSCF_{113}$ thin films (~62.5 nm) on YSZ with a ~5 nm gadolinium-doped ceria (GDC, 20 mol % Gd) as the buffer layer to prevent the formation of $La_2Zr_2O_7$.[35] Varying thicknesses of LSC_{214} (~0.26, ~0.78, ~2.6, and ~5 nm) were deposited subsequently on top of the $LSCF_{113}$/GDC/YSZ.

The epitaxial LSC_{113} thin films (~85 nm) with and without LSC_{214} decoration (~2.6 nm) were also prepared on YSZ(001) with a GDC buffer layer using PLD. Details for the $LSCF_{113}$, LSC_{214}, LSC_{113}, and GDC PLD target syntheses and PLD deposition process can be found in the Electronic Supplementary Information (ESI†).

2.2 High resolution X-ray diffraction (HRXRD)

Oxide phase purity and orientation of the thin film systems were investigated via high resolution X-ray diffraction (HRXRD) using a four-circle diffractometer (PANalytical, USA and Bruker D8, Germany). Measurements were performed in normal and off-normal configurations. The in-plane lattice parameters (***a*** lattice parameter) of $LSCF_{113}$ and LSC_{113} was determined from the off-normal $(202)_{pc}$ peak position (where "pc" denotes the pseudocubic notation) and the ***c*** lattice parameter of $LSCF_{113}$ and LSC_{113} normal to the film surface was determined from the $(002)_{pc}$ peak position. Surface morphology was examined by optical microscopy (Carl Zeiss, Germany) and atomic force microscopy (AFM) (Veeco, USA). AFM images of as-deposited $LSCF_{113}$ and LSC_{214}-decorated $LSCF_{113}$ films revealed that the surfaces were smooth with the root-mean-square (RMS) roughness values of 0.237 – 0.323 nm, as shown in Fig. S1†. Indeed, those of as-deposited LSC_{113} and LSC_{214}-decorated LSC_{113} films also showed vey smooth surfaces with the RMS roughness values of 0.769 – 1.133 nm, as shown in Fig. 5. The RMS roughness was comparable across all surfaces.

2.3 Electrochemical impedance spectroscopy (EIS)

Electrochemical impedance spectroscopy (EIS) measurements of microelectrodes ~200 μm in diameter were performed using a microprobe station (Karl Süss, Germany) connected to a

frequency response analyzer (Solartron 1260, USA) and dielectric interface (Solartron 1296, USA). Temperature was controlled at 550 °C with heating stage (Linkam TS1500, UK) and data were collected between 1 MHz to 1 mHz using a voltage amplitude of 10 mV. EIS testing temperature was calibrated with a thermocouple contacting the thin film surface and deviation of ± 5 °C was observed. EIS experiments were completed between $p(O_2)$ of 10^{-3} atm and 1 atm. EIS data were analyzed using an equivalent circuit (Fig. S4b†), from which the ORR resistance (R_{ORR}) and surface exchange rate were obtained. Details about the EIS testing procedure, data analysis, and c_0 estimation can be found in the ESI†.

2.4 Auger electron spectroscopy (AES)

Auger electron spectroscopy (AES) was conducted using a Physical Electronics 700 Scanning Auger Nanoprobe (PHI, USA) operating at an accelerating voltage of 10 kV to analyze the surface chemistry change of the LSC_{214}-decorated $LSCF_{113}$ and the LSC_{214}-derocated LSC_{113} films after heat treatment. The films were annealed at 550 °C for 6 hours in an oxygen partial pressure of 1 atm before AES data were collected. The AES data were collected using two different modes: area mode (three different 10 μm × 10 μm regions selected across a sample) and point mode (two different ~0.45 μm diameter spots selected on a sample) in an ultra-high vacuum chamber. Elemental quantification of AES spectra utilized relative sensitivity factors (RSFs) of 0.059, 0.027, 0.076, 0.178, and 0.212 for La_{MNN}, Sr_{LMM}, Co_{LMM}, Fe_{LMM}, and O_{KLL}, respectively, as supplied by the AES manufacturer (Physical Electronics). Details about AES measurement and analysis can be found in the ESI†.

2.5 Density functional theory (DFT)

Spin polarized Density Functional Theory (DFT) calculations are preformed with the Vienna *Ab-initio* Simulation Package[36, 37] using the Projector-Augmented plane-Wave method.[38] Exchange-correlation is treated in the Perdew-Wang-91[39] Generalized Gradient Approximation (GGA). The GGA+*U* calculations[40] are performed with the simplified spherically averaged approach,[41] where the U_{eff} (U_{eff} = Coulomb *U* - exchange *J*) is applied to *d* electrons. (U_{eff}(Fe) = 4.0 eV and U_{eff}(Co) = 3.3 eV).[25, 42] All calculations are performed in the ferromagnetic state in order to use a consistent and tractable set of magnetic structures.

Calculations for Sr_{La} substitution energies in bulk LSC_{113} and $LSCF_{113}$ are simulated using a $2a_{pv}\times2a_{pv}\times2a_{pv}$ pseudocubic supercell structure of $La_{0.75}Sr_{0.25}CoO_3$ (with $a_{pv}(La_{0.75}Sr_{0.25}CoO_3)$ = 3.88 Å, where a_{pv} is the relaxed GGA+U perovskite lattice constant) and $La_{0.625}Sr_{0.375}Fe_{0.75}Co_{0.25}O_3$ (a_{pv} ($LSCF_{113}$) = 3.91 Å) with 2×2×2 k-point mesh and 450 eV plane-wave energy cut-off. Sr_{La} substitution energy in bulk LSC_{214} is simulated using a $2a_{rp}\times2a_{rp}\times c_{rp}$ supercell structure of LSC_{214} (where a_{rp} and c_{rp} are the relaxed GGA+U RP phase lattice constant: $a_{rp}(LSC_{214})$ = 3.86 Å, $c_{rp}(LSC_{214})$ = 12.50 Å).[43] The supercell configurations are illustrated in Fig. S8†. The Sr_{La} substitution energy for $La_{0.75}Sr_{0.25}CoO_3$ ($La_{0.625}Sr_{0.375}Fe_{0.75}Co_{0.25}O_3$) bulk was taken as the difference in energies between a $La_{0.625}Sr_{0.375}CoO_3$ ($La_{0.5}Sr_{0.5}Fe_{0.75}Co_{0.25}O_3$) bulk and a $La_{0.75}Sr_{0.25}CoO_3$ ($La_{0.625}Sr_{0.375}Fe_{0.75}Co_{0.25}O_3$) bulk. Similarly, the Sr_{La} substitution energy for LSC_{214} was calculated using the total energy difference between $(La_{0.5}Sr_{0.5})_2CoO_4$ and $(La_{0.4375}Sr_{0.5625})_2CoO_4$.

The LSC_{214}-$LSCF_{113}$ heterointerface was simulated with a periodic 176-atom supercell ($2a_{113}\times2a_{113}$ supercell in the x-y plane (a_{113} = $a_{pv}(LSCF_{113})$ =3.91 Å) with 12-layers of $La_{0.625}Sr_{0.375}Fe_{0.75}Co_{0.25}O_3$ and 6-layers of LSC_{214} along *z* where the relaxed $c_{rp}(LSC_{214})$=12.42 Å). The LSC_{214}-$LSCF_{113}$ heterointerface calculations and structural model were adopted based on

those reported previously for LSC_{214}-LSC_{113}.[24, 25] Three different Sr/La and Co/Fe arrangements in the LSC_{214}-$LSCF_{113}$ interface model are investigated, as shown in Fig. S8†.

Ab initio thermodynamic analysis for LSC_{113} and $LSCF_{113}$ surface stability are simulated using the 9-layer 2×2 symmetric (001) AO terminated and BO_2 terminated slabs with the central 5 layers fixed to a composition close to the bulk LSC_{113} and $LSCF_{113}$. The La/Sr (and Fe/Co for $LSCF_{113}$) content of the top two and bottom two layers are varied, as illustrated in Fig. S11†. $LaSrCoO_4$ surface calculations are performed using the 9-layer 2×2 symmetric (001) AO terminated and 8-layer (100) A_2BO_4 terminated slabs with the top and bottom surface layers varying the A-site Sr concentration and the rest of the slab composition fixed to $LaSrCoO_4$, as also illustrated in Fig. S11†. More details of the *ab initio* methods and thermodynamic analysis are provided in the ESI†.

3. Results and Discussion

3.1 Structural relationship of epitaxial $LSCF_{113}$ thin films with LSC_{214} decoration

Normal XRD data (Fig. 1) of the undecorated $LSCF_{113}$ and LSC_{214}-decorated $LSCF_{113}$ films clearly show the presence of the $(00l)_{pc}$ (l is integer) peaks of $LSCF_{113}$ and $(00l)_{cubic}$ (l is even) peaks of GDC and YSZ, indicating that the $LSCF_{113}$ film grew epitaxially with the following epitaxial relationships: $(001)_{pc}LSCF_{113}$ // $(001)_{cubic}GDC$ // $(001)_{cubic}YSZ$. With LSC_{214} coverage equal to ~5 nm in thickness, the $(00l)_{tetra.}$ (l is integer) peaks of LSC_{214} become visible, which represents $(001)_{tetra.}LSC_{214}$ // $(001)_{pc}LSCF_{113}$ // $(001)_{cubic}GDC$ // $(001)_{cubic}YSZ$. The subscript "tetra." denotes the tetragonal notation.[44, 45] Off-normal phi-scan analysis of the undecorated $LSCF_{113}$ and LSC_{214}-decorated $LSCF_{113}$ films shows that LSC_{214} $\{103\}_{tetra.}$, LSC_{113}

$\{101\}_{pc}$, GDC $\{202\}_{cubic}$ and YSZ $\{202\}_{cubic}$ have strong peaks with 4-fold cubic symmetry (Fig. 1b), which reveal the in-plane crystallographic relationships between GDC and YSZ (a cube-on-cube alignment), $LSCF_{113}$ and GDC (an in-plane 45º rotation with $[100]_{pc}LSCF_{113}$ // $[110]_{cubic}GDC$ // $[110]_{cubic}YSZ$), and $LSCF_{113}$ and LSC_{214} (no rotation with $[100]_{pc}LSCF_{113}$ // $[100]_{tetra.}LSC_{214}$), as shown in Fig. 1c. The undecorated LSC_{113} and LSC_{214}-decorated LSC_{113} thin films also had the same crystallographic relationships as shown in Fig. S2†. Similar to our previous studies,[22, 23, 46] the relaxed lattice parameters, $\hat{a}$ of the epitaxial $LSCF_{113}$ films with and without LSC_{214} surface decoration in this study at room temperature did not change significantly with different LSC_{214} decoration thicknesses, ranging from 3.902 – 3.906 Å (Fig. S3a†). The $\hat{a}$ of the epitaxial LSC_{113} films with and without LSC_{214} surface decoration was also found not to change significantly, having 3.838 – 3.839 Å (Fig. S3a†). As shown in Fig. S3b†, both in-plane and out-of-plane strains of $LSCF_{113}$ and LSC_{113} films were not strongly influenced by the LSC_{214} coverage, which is supported by the fact that the lattice constant of LSC_{214} ($a_{tetra.} \approx 3.819$ Å for LSC_{214} bulk[47]) is very close to that of $LSCF_{113}$ ($a_{tetra.} \approx 3.885$ Å for $LSCF_{113}$ bulk[19]) and LSC_{113} ($a_{tetra.} \approx 3.854$ Å for LSC_{113} bulk[48]). This observation is further supported by our recent work,[23] where the LSC_{214} decoration has no influence on the in-plane and out-of-plane strains of the epitaxial LSC_{113} films at elevated temperatures. Details about lattice parameter calculation and HRXRD of LSC_{214}-decorated LSC_{113} film can be found in the ESI†.

3.2 Oxygen surface exchange kinetics of the $LSCF_{113}$ and LSC_{113} with and without LSC_{214} decoration

EIS data collected from the undecorated $LSCF_{113}$ and LSC_{214}-decorated $LSCF_{113}$ films at 550 °C with an oxygen partial pressure of 1 atm are shown in Fig. 2a. The real impedance of the

predominant semicircle decreased slightly with LSC_{214} coverage. In addition, the predominant semicircle was found to increase with decreasing oxygen partial pressure, where EIS data of all samples used in this study were found to show nearly perfect semicircle impedances.[49] Representative EIS data collected from the $LSCF_{113}$ film with ~5 nm LSC_{214} coverage measured at 550 °C as a function of $p(O_2)$ are shown in Fig. 2b. Considering the fact that the film thicknesses are much smaller than the critical thickness for bulk transport limitation (estimated to 3.28 μm for bulk $LSCF_{113}$ at 550 °C[50]), the ORR kinetics are limited by surface oxygen exchange but not by oxygen ion diffusion. This observation is in agreement with the $p(O_2)$-dependent impedance responses, as expected for a surface oxygen exchange kinetics limited electrode.[46, 51-53] Similar to $LSCF_{113}$ thin films, LSC_{214}-decorated LSC_{113} thin film, where the film thicknesses are much smaller than the critical thickness (estimated to 1 μm for bulk LSC_{113} at 550 °C[6]), also showed the $p(O_2)$-dependent impedance responses (Fig. S5†), suggesting that the oxygen surface exchange kinetics governs the oxygen electrocatalysis on the film surface.

The k^q of the undecorated $LSCF_{113}$ was found to be higher than that of the undecorated LSC_{113}, which is in good agreement with our previous experimental studies and consistent with recent trends correlated k^q with the bulk oxygen *p*-band center,[54] which is found to be higher in the $LSCF_{113}$ than the LSC_{113}. It should be noted that LSC_{214} coverage led to only 1 – 2 times enhancement of the k^q values of the undecorated $LSCF_{113}$ thin films while the k^q of LSC_{113} with LSC_{214} coverage was found to be nearly 2 orders of magnitude higher than that of the undecorated LSC_{113}. As Han et al. have proposed that both the anisotropy of LSC_{214} and the lattice strain near the interface between LSC_{214} and LSC_{113} are responsible for the significantly enhanced surface exchange kinetics of heterostructred oxide interface,[26] we also examined the average strains in the films. However, LSC_{214} decoration had no detectable influence on the

average strains of either $LSCF_{113}$ or LSC_{113} films, as shown in Fig. S3†, suggesting that strain was not playing a critical role in these samples.

The volume specific capacitances (*VSCs*) of the $LSCF_{113}$ and LSC_{113} films, corresponding to the change in the oxygen nonstoichiometry (δ) induced by the change in the electrical potential, did not change significantly with LSC_{214} surface coverage, as shown in Fig. 2d. This result is in good agreement with our previous results[22] where LSC_{214} surface coverage has no influence on the oxygen vacancy concentration of LSC_{113} thin films. Moreover, the *VSCs* of LSC_{113} with and without LSC_{214} decoration in this study were comparable to those of epitaxial LSC_{113} thin films reported previously.[53] This result indicates that the oxygen content in the LSC_{113} and $LSCF_{113}$ films with and without LSC_{214} coverage do not contribute to the modification of the k^q values observed, suggesting that the changes in k^q values are due to changes in surface chemistry. Details of *VSCs* are provided in the ESI†.

The LSC_{214} decoration can also greatly reduce the time-dependent degradation of the oxygen surface exchange kinetics of the LSC_{113} thin film, as shown in Fig. 3a. After annealing at 550 °C for 70 hours, the k^q values of the undecorated LSC_{113} was found to significantly decrease as annealing time increases, consistent with results shown by Kubicek, et al.,[55] while LSC_{214}-decorated LSC_{113} showed a relatively small reduction in the k^q values after 70 hours annealing. In contrast, LSC_{214} decoration had no influence on preventing the time-dependent degradation of the oxygen surface exchange kinetics of the $LSCF_{113}$ thin film (Fig. 3b). Regardless of the LSC_{214} decoration, the time-dependent degradation of the oxygen surface exchange kinetics of the $LSCF_{113}$ thin films was found to show similar reduction in the k^q values as a function of annealing time. The *VSCs* of the LSC_{113} and $LSCF_{113}$ with and without LSC_{214} coverage was found to not change significantly with increasing the annealing time (Fig. S6†), which indicates

that the degradation of the oxygen surface exchange kinetics as a function of time does not depend on the bulk oxygen content.

3.3 Surface chemistry and stability changes of the $LSCF_{113}$ and LSC_{113} with and without LSC_{214} decoration

The changes in the surface chemistry of LSC_{113} and $LSCF_{113}$ films without and with LSC_{214} decoration before and after annealing at 550 °C for 6 hours were revealed by Auger electron spectroscopy (AES) using area mode (three different 10 μm × 10 μm regions selected across a sample), as shown in Fig. 4. La Auger signals of the undecorated LSC_{113} surface were found to decrease with LSC_{214} coverage (Fig. 4a) while Sr Auger signals were found to increase (Fig. 4b). In contrast, the changes in La and Sr Auger signals of $LSCF_{113}$ film surfaces with and without LSC_{214} coverage were considerably smaller than those observed for LSC_{113} (negligible changes noted for Sr Auger), as shown in Figs. 4c and 4d. LSC_{214} decoration led to a greater increase in the Sr/La ratio for the LSC_{214}-decorated LSC_{113} surface than LSC_{214}-decorated $LSCF_{113}$, as shown in Fig. 4f. The large increase in the surface Sr/La ratio for LSC_{214}-decorated LSC_{113} relative to LSC_{113} is in good agreement with our recent COBRA and DFT studies,[24] which reveals pronounced strontium (Sr) segregation at the interface of LSC_{113} and LSC_{214} and near the surface of LSC_{214}. The surface Sr concentration of the LSC_{113} and $LSCF_{113}$ modulated by LSC_{214} coverage can be associated with a change in the oxygen 2*p* band center (relative to the Fermi level), which can contribute to the enhancement of the oxygen surface exchange kinetics. This hypothesis will be explored with DFT calculations and further discussed in section 3.6.

The LSC_{214} decoration was found to influence the surface stability of LSC_{113} and $LSCF_{113}$ at elevated temperatures. AFM imaging revealed that as-deposited LSC_{113} with and

without LSC_{214} coverage had nearly atomically flat surfaces with RMS roughness ~1 nm, having no discrete particles on the surfaces before annealing, as shown in Fig. 5b and 5c. After annealing at 550 °C for 6 hours, discrete particles, which have higher Sr Auger signals (Fig. S7†) than the rest of the surface as well as the surfaces before annealing, were noted on the undecorated LSC_{113} (Fig. 5f). This observation is consistent with our recent *in situ* X-ray reflectivity (XRR) studies of surface structure and chemistry changes of LSC_{113} films[23] and detection of Sr-enriched particles on the film surface from *in situ* ambient pressure X-ray photoelectron spectroscopy measurements.[34, 56] It has been proposed that LSC_{113} surface decomposes to SrO-like, $(La_{1-x}Sr_x)_2CoO_4$-like, and CoO_x-like phases with increasing temperature.[57, 58] In contrast to LSC_{113}, no particles were found on the LSC_{214}-decorated LSC_{113} surface after annealing for 6 hours, which indicates that LSC_{214} decoration can stabilize the LSC_{113} surface, and suppress the formation of Sr-enriched particles on the LSC_{113} surface. In contrast, no particles was found on the $LSCF_{113}$ surface with and without LSC_{214} coverage after annealing at 550 °C for 6 hours (Fig. 5h and 5i), which suggests that the (001) $LSCF_{113}$ surface is thermodynamically more stable against decomposition than that of LSC_{113} at elevated temperatures. The physical origins of the observed different surface stability may be attributed to the thermodynamic stability of the LSC_{113} and $LSCF_{113}$ with and without LSC_{214} coverage, which will be explored with *ab initio* DFT modeling in section 3.4.

Modulating surface chemistry by perturbing chemical potentials of elements near the surfaces region with LSC_{214} decoration can influence the surface stability (Fig. 5) of LSC_{214}-decorated LSC_{113} and $LSCF_{113}$ films. Discrete particles, which have higher Sr Auger signals (Fig. 5a), form on the surfaces of all samples after annealing for 70 hours, as shown in Fig. 5. The chemistry of these Sr-enriched particles is not well understood. In the case of the undecorated

LSC_{113}, however, recent COBRA experiments suggest that these Sr-enriched particles on the LSC_{113} thin films have a composition approaching to that of $SrCoO_{3-\delta}$,[59] which is likely to coexist with or decompose to secondary phases such as $SrO/Sr(OH)_2/SrCO_3$[60, 61] and $(La,Sr)_2CoO_{4\pm\delta}$,[62] leading to surface passivation for the oxygen exchange kinetics.[63] Similar to the LSC_{113}, $LSCF_{113}$ can decompose into A_2BO_4[18] after annealing over 16 hours and is also susceptible to the formation of the surface Sr-enriched particles,[64] which contribute to degradation of cell performance.[65] As the Sr spectra of the particles on the LSC_{214}-decorated LSC_{113} was found to resemble that of an as-deposited LSC_{214} sample prepared by PLD, it is postulated that the discrete particles on the LSC_{214}-decorated LSC_{113} result from agglomeration of LSC_{214} coverage,[66] which reduces active heterointerface region,[22] and/or the decomposition of the LSC_{113} and LSC_{214} coverage[67] induced by higher Sr concentration through the cation interdiffusion for long annealing time, leading to reduction in the k^q values after 70 hours annealing for the LSC_{214}-decorated LSC_{113}. In the case of the LSC_{214}-decorated $LSCF_{113}$, the particles may also be attributed to decomposition of both $LSCF_{113}$[18] and LSC_{214} or agglomeration of LSC_{214} coverage, which can be supported by the AES Sr spectra having a similar intensity and shape as shown in the particles on the $LSCF_{113}$.

The changes in the surface chemistry by LSC_{214} coverage can also be responsible for the observed time-dependent oxygen surface exchange kinetics of the LSC_{214}-decorated LSC_{113} and $LSCF_{113}$ films, as shown in Fig. 3. The formation of surface Sr-enriched particles can lead to the reduction in the surface exchange kinetics of LSC_{113}[27, 55] and result from the decomposition of $LSCF_{113}$.[64, 68] The LSC_{113} thin film without LSC_{214} decoration was found to show discrete particles on the surface after annealing at 550 °C for 6 hours, in which the k^q values were reduced by ~1 order of magnitude. After 70 hours, the increased number density of discrete

particles was accompanied by a reduction in k^q (~2 orders of magnitude). It is noted that no particles were observed on the surface of LSC_{214}-decorated LSC_{113}, where the k^q values showed negligible changes after annealing for 6 hours and relatively small degradation of the k^q values was found after 70 hours annealing. This observation suggests that LSC_{214} coverage can retard the time-dependent degradation of the oxygen surface exchange kinetics of the LSC_{113} thin film, suppressing the formation of the Sr-enriched secondary particles on the surface. In contrast to the LSC_{113} thin films, LSC_{214} decoration was found to have no influence on the time-dependent oxygen surface exchange kinetics of $LSCF_{113}$, showing similar k^q values regardless of the LSC_{214} coverage. Furthermore, LSC_{214} decoration was also found to have no influence on suppressing the formation of the Sr-enriched particles on the surface of $LSCF_{113}$. It is hypothesized that $LSCF_{113}$ has higher stability against decomposition than that of LSC_{113}, and therefore LSC_{214} cannot contribute the enhancement of the $LSCF_{113}$ stability, resulting in negligible k^q enhancement after 70 hours annealing. DFT modeling and thermodynamic analysis can support this hypothesis, which will be discussed in section 3.7.

It is noted that the effects of cathode polarization can also influence on the kinetics and stability of the cathode materials and their heterointerfaces, as also revealed in our previous work.[34, 57] In this work, we focus on investigating how differently the heterostructured interface can influence on the surface exchange kinetics and surface stability within two different model systems, while the effect of polarization on the kinetics and stability of the heterostructured interface will be further studied in a separate work.

In the following sections, we discuss *ab initio* DFT modeling and thermodynamic analysis performed to investigate LSC_{113} and $LSCF_{113}$ (001) surface stability with respect to the concentration of Sr in the top surface layer, relative stability for the Sr substitution of La (Sr_{La}) in

bulk LSC_{113}, LSC_{214}, $LSCF_{113}$, and at the LSC_{214}-$LSCF_{113}$ heterointerfaces, and assessment of surface stability against particle formation through decomposition reaction free energy of fully Sr surface substituted (*i.e.*, SrO terminated) LSC_{113}, $LSCF_{113}$ and LSC_{214} to form lower order binary metal oxides or to form the RP phase with Co_3O_4.

3.4 *ab initio* thermodynamic assessment of stable Sr content for the $LSCF_{113}$ and LSC_{113} (001) surfaces and LSC_{214} (001) and (100) surfaces

To probe the physical origin of experimentally observed surface chemistry changes in Fig. 3, *ab initio* thermodynamic analysis was performed to investigate the stability of the LSC_{113} and $LSCF_{113}$ unreconstructed (001) surfaces vs. surface termination (*i.e.*, the AO and BO_2 surfaces) with varying cation content (La-Sr content for both LSC_{113} and $LSCF_{113}$ and Fe-Co content for $LSCF_{113}$), as well as stability of the LSC_{214} (001) and (100) surface terminations at varying surface layer La-Sr concentration. It is noted that the adopted DFT models in this work are limited to describe stability of the top two surface layers at varying dopant content within the perovskite phase (or within the RP phase in case of LSC_{214}). Chemical inhomogeneity near the surfaces, including formation of Sr-enriched secondary phases on the surfaces and in extended region beneath the surface terminations[69, 70] is not directly addressed in the *ab initio* thermodynamic analysis performed here. While being aware of the limitation of the adopted thermodynamic model, predicted stable surface Sr content among various material systems can be useful for trend discussions in comparisons with experimental measurements.

In this work, we focus on results for T = 550 °C and $p(O_2)$ = 1 atm (details of the *ab initio* methods and the thermodynamic analysis are provided in the ESI†). Within the LSC_{113} bulk stability region set by chemical potential boundaries of thermodynamic equilibrium

between the LSC_{113} bulk and relevant lower order oxides (specifically, SrO, La_2O_3, Co_3O_4, perovskite $LaCoO_3$, and brownmillerite $SrCoO_{2.5}$), the *ab initio* thermodynamic analysis predicts that the most stable LSC_{113} (001) surface among the investigated (001) surface configurations is the AO surface containing ~75% Sr concentration on the A site, as shown in Fig. 6a. In addition, upon further increasing $p(O_2)$ to 50 atm (which corresponds to increase of oxygen chemical potential by 0.13 eV per O), the predicted stable (001) surface layer Sr content within stable bulk region is found to span over both the ~75% and 100% Sr concentration in the contour plot (Fig. S12b†), while decreasing $p(O_2)$ to 0.05 atm (which corresponds to decrease of oxygen chemical potential by 0.10 eV per O) causes the predicted stable bulk region (with the (001) AO surface containing 75% Sr concentration on the A site as the stable surface) to be shifted farther away from the area in the contour plot where the (001) AO surface layer containing 100% Sr concentration is stable (red color in the contour plot), as shown in Fig. S12c†. The increasingly stable surface Sr content with increasing $p(O_2)$ is consistent with the reported $p(O_2)$ dependence in surface Sr enrichment of Sr-doped $LaMnO_3$ and $LSCF_{113}$ perovskites,[64, 71] and results from minimization of surface free energy in responding to relative metal chemical potential changes in the bulk perovskites upon change of oxygen chemical potential. This origin is in contrast to the previously proposed model based on point defect stability vs. $p(O_2)$ and their interactions with the Sr dopant (attraction for oxygen vacancy and repulsion for cation vacancies) proposed by Lee et al.[71] and Crumlin et al..[56]

The surface phase diagrams of the stable (001) surface layer (including stable termination and Sr/La and Fe/Co concentrations) for the condition of effective Fe chemical potential in $LSCF_{113}$ equal to -0.12 eV relative to that of Fe_2O_3 are shown in Fig. 6b and 6c for $LSCF_{113}$ (001). The definition of the effective Fe chemical potential is described in the ESI†, and a

complete set of surface phase diagrams at different effective Fe chemical potentials are provided in Fig. S13† ($\Delta\mu^{eff}_{Fe}(La_{0.625}Sr_{0.375}Fe_{0.75}Co_{0.25}O_3)$ = 0.0 eV 0.0, -0.24, -0.36 eV vs. μ^{eff}_{Fe} (Fe_2O_3), as shown in Fig. S13a†, S13c†, and S13d†). The two independent effective metal chemical potentials are represented by $\Delta\mu^{eff}_{Co}(La_{0.625}Sr_{0.375}Fe_{0.75}Co_{0.25}O_3)$ and $\Delta\mu^{eff}_{Sr}(La_{0.625}Sr_{0.375}Fe_{0.75}Co_{0.25}O_3)$, where $\Delta\mu^{eff}_{Co}(La_{0.625}Sr_{0.375}Fe_{0.75}Co_{0.25}O_3) = \mu^{eff}_{Co}(La_{0.625}Sr_{0.375}Fe_{0.75}Co_{0.25}O_3) - \mu^{eff}_{Co}(Co_3O_4)$ and $\Delta\mu^{eff}_{Sr}(La_{0.625}Sr_{0.375}Fe_{0.75}Co_{0.25}O_3) = \mu^{eff}_{Sr}(La_{0.625}Sr_{0.375}Fe_{0.75}Co_{0.25}O_3) - \mu^{eff}_{Sr}(SrO)$. The $La_{0.625}Sr_{0.375}Fe_{0.75}Co_{0.25}O_3$ (001) surface stability analysis results predicts that the most stable surfaces are the AO surfaces with the surface layer A-site Sr concentration equal to 100% within the region of chemical potentials where the bulk material is stable relative to the lower order oxides (Fig. 6b). Such a conclusion holds for all the other investigated conditions of Fe chemical potentials, as shown in Fig. S13a†, S13c†, and S13d†. The predicted Sr concentrations can be combined with stability analysis to show that our predictions are consistent with the stability differences between (La,Sr)FeO_3 and (La,Sr)CoO_3 perovskites described in previous study[72] (for more details see section 3.7). The predicted $LSCF_{113}$ (001) surface stability results based on our *ab initio* thermodynamic analysis are in good agreement with a recent Low Energy Ion Scattering study on $LSCF_{113}$ pellets,[73] which reports the disappearance of the transition metal ions and increased Sr coverage on the $LSCF_{113}$ surfaces upon annealing in air at 600 °C and 800 °C.

Although the Sr segregation is quite robustly predicted, the results for Co/Fe segregation in $LSCF_{113}$ are more ambiguous (Fig. 6c and S13†). The ambiguity is due to the fact that the chemical potential of Co/Fe is only constrained to a range of values by the restriction of having stable bulk $LSCF_{113}$. Within this range of values the most stable (sub)-surface layer Co/Fe concentration varies from about 0-50%, depending on the chemical potential of Co/Fe within the

stable bulk $LSCF_{113}$ region (Fig. S13†).

A similar surface stability analysis as described above was also performed for the LSC_{214} surfaces (Fig. 6d), with varying A-site La/Sr content for the top surfaces. Due to the anisotropic nature of the RP phases the two surfaces, (001) and (100), were both considered. In fact, these two surface terminations have been shown to exhibit distinct surface exchange activities[45, 74] while various Sr doping concentration can also lead to changes in their relative surface stability.[45] Our *ab initio* thermodynamic analysis predicts that at $p(O_2)$ = 1 atm and T = 550 °C the fully Sr enriched (001) AO surface is the most stable surface between the investigated (001) AO and (100) A_2BO_4 surface configurations within the bulk LSC_{214} stability region. In addition, the (100) A_2BO_4 surfaces are predicted to be stable with fully enriched surface layer Sr at the A-sites within the (100) surface orientation. Comparatively, the surface energy of the fully Sr-enriched (100) A_2BO_4 surface is found to be a factor of 1.2 ~ 2 greater than the surface energy of the fully Sr-enriched (001) AO surface within the stable bulk $LaSrCoO_4$ region, suggesting the greater stability of the (001) AO surface with fully enriched Sr vs. the (100) A_2BO_4 surfaces.

Overall, our results suggests that at the experimental condition investigated in this work (i.e., T = 550 °C and $p(O_2)$ = 1 atm), both the stable $LSCF_{113}$ and LSC_{214} (001) surfaces can exhibit higher Sr concentration than the LSC_{113} (001) surfaces. The predicted stable surface Sr content among $LSCF_{113}$, LSC_{113}, and LSC_{214}, along with the calculated *ab initio* Sr_{La} substitution energies in bulk LSC_{113}, $LSCF_{113}$, LSC_{214}, and their interfaces, are in accordance with the experimental trend in surface Sr Auger signals of the AES measurements shown in Fig. 4, as discussed previously in section 3.3.

3.5 *Ab initio* Sr_{La} substitution energies in bulk LSC_{214}, LSC_{113}, $LSCF_{113}$, and the LSC_{214}-

decorated $LSCF_{113}$ heterointerfaces

To understand the physical origin of different enhancement on the surface Sr content in the $LSCF_{113}$ and LSC_{113} films upon LSC_{214} decoration, *ab initio* DFT calculations were performed to investigate energy for Sr substitution of La (Sr_{La}) in the structures of LSC_{214}, LSC_{113}, and $LSCF_{113}$, as shown in Fig. 7a (details of the DFT modeling approaches are provided in the ESI†). The calculated Sr_{La} substitution energies in relaxed bulk LSC_{214}, LSC_{113}, and $LSCF_{113}$ (all relative to that of LSC_{113}) suggest a weaker thermodynamic driving force (-0.12 eV) for Sr interdiffusion from $LSCF_{113}$ to LSC_{214} than from LSC_{113} to LSC_{214} (-0.7 eV). This finding is supported by the AES results in Fig. 4f, where the LSC_{214}-decorated $LSCF_{113}$ surface exhibits only a slight increase in the Sr/La ratio relative to $LSCF_{113}$ in contrast to significantly more enhanced Sr/La ratio on the surface of LSC_{214}-decorated LSC_{113} relative to LSC_{113}. To further understand the interfacial effect on the Sr_{La} substitution energies, three LSC_{214}-$LSCF_{113}$ interface configurations with different Sr/La and Co/Fe arrangements were investigated (more detailed information of the interface models is provided in the ESI†), as shown in Fig. 7b. The most stable Sr_{La} substitution was found to be in the first interface layer adjacent to the $LSCF_{113}$ region (the interfacial region is labeled with the gray dotted line). Moving from this interface layer with the most stable Sr_{La} substitution toward the $LSCF_{113}$ and LSC_{214} regions, the Sr_{La} substitution energies become destabilized and gradually approach to the bulk $LSCF_{113}$ and LSC_{214} values. The Sr_{La} stability across the LSC_{214}-$LSCF_{113}$ interface can depend on cation configurations and there is no clear trend for Sr segregation to the interface, as shown in Fig. 7b, which can be attributed largely to the small Sr_{La} substitution energy gain (~0.2 eV) from bulk $LSCF_{113}$ to bulk LSC_{214}. In contrast, there is a more clear energetic trend for the LSC_{113}-LSC_{214} interface,[25] where Sr_{La} substitution becomes monotonically more stabilized moving from the LSC_{113} toward the

LSC_{214} region, which can be attributed to the ~1 eV difference in the relative Sr_{La} stability between the bulk LSC_{113} and LSC_{214}. The energies in Fig. 7b represent thermodynamic driving forces of Sr_{La} substitution (relative to the bulk LSC_{113}) for the simulated configurations close to the nominal bulk phase composition, rather than the equilibrated interfacial configurations. We note that the as-grown $LSCF_{113}$ film surfaces may be initially Sr enriched,[75] and consequently the thermodynamic driving force for Sr_{La} interdiffusion from the decorated LSC_{214} phase back to the Sr-enriched LSC_{214}-$LSCF_{113}$ interfaces is expected to be reduced as compared to the energetic results shown in Fig. 7b.

In comparison with the experimental observations, here we use the *ab initio* modeling of the thermodynamically stable $LSCF_{113}$, LSC_{113}, and LSC_{214} surfaces, the thermodynamic driving forces for Sr_{La} substitution in bulk LSC_{113}, LSC_{214}, and $LSCF_{113}$ as well as the LSC_{214}-LSC_{113} and LSC_{214}-$LSCF_{113}$ heterointerfaces, to discuss possible physical origins leading to the different stability for the (001) LSC_{113} and $LSCF_{113}$ surfaces with and without LSC_{214} decoration. DFT computed thermodynamic driving forces of Sr_{La} substitution from the LSC_{113} to interface of LSC_{113} and LSC_{214}, and to the LSC_{214} in bulk and on the surface[29, 30] show that LSC_{214} decorated on LSC_{113} acts as a Sr sink, which is in agreement with the strong Sr segregation seen in these systems, from ~60% Sr at the LSC_{113} film surfaces without the LSC_{214} decoration to up to ~100% Sr at the LSC_{214}-on-LSC_{113} interface and in the LSC_{214} bulk and on the surface.[24] The Sr redistribution in LSC_{214}-on-LSC_{113} interface films was further attributed to be responsible for the enhanced surface exchange activity, based on the upshift of the O *2p* band centers with increasing Sr content at the interface and surface of LSC_{214}-on-LSC_{113}, as will be discussed below in section 3.6. In addition, the greater stability of LSC_{214}-on-LSC_{113} vs. LSC_{113} with respect to surface Sr-enriched particle formation may be associated with the fact that the

$(La,Sr)CoO_4$ RP phase occurs as a $La_{1-x}Sr_xCoO_{3-\delta}$ decomposition product or intermediate in relatively reducing environments.[58, 76] Considering the LSC_{113} decomposition reaction to form LSC_{214}, when adding more LSC_{214} decomposition product at the LSC_{113} surfaces may reduce the thermodynamic driving force of the LSC_{113} decomposition reaction to form LSC_{214} and stabilize the perovskite phase, as will also be discussed in section 3.7. Therefore, surface decoration with the LSC_{214} phase may suppress the precipitation of the secondary particles on the LSC_{113} surface resulting in stabilizing the perovskite phase. Similar observation of disappearance of Sr-enriched secondary phase formation on surfaces of $La_{0.6}Sr_{0.4}CoO_{3-\delta}$ films with $(La,Sr)CoO_4$ powders was also reported by Unemoto et al.[31] In contrast, the computed DFT of Sr_{La} substitution energies from the $LSCF_{113}$ to interface of $LSCF_{113}$ and LSC_{214} are closer than those of LSC_{113} vs. LSC_{214}, and the stable $LSCF_{113}$ (001) surface is predicted to fully Sr enriched. Therefore, the comparable Sr_{La} stability between $LSCF_{113}$ and LSC_{214} results in weaker thermodynamic driving force on modifying the surface chemistry (Sr content) of $LSCF_{113}$ upon LSC_{214} decoration. In addition, as will be shown in section 3.7, the DFT computed formation energies (relative to the binary metal oxides) of the $LSCF_{113}$ and the LSC_{214} at full Sr substitution also suggest that both exhibit comparable stability against decomposition, consistent with the amount of surface particle formation upon annealing with time for $LSCF_{113}$ without and with LSC_{214} decoration (Fig. 5).

3.6 Electronic structure changes of the $LSCF_{113}$ and LSC_{113} with and without LSC_{214} decoration

The large and small surface exchange kinetics enhancement observed for LSC_{214} decoration on LSC_{113} and $LSCF_{113}$ film can be attributed to large and small upshift of the oxygen 2*p* band center relative to the Fermi level, respectively. Increasing Sr concentration on the A-site

in the perovskite phases has been shown to lead to upshift of the oxygen 2*p* band center relative to the Fermi level[54, 77], which correlates with the increased surface oxygen exchange kinetics. In addition, our previous work[24] has proposed that the upshift of the oxygen 2*p* band centers with pronounced Sr segregation can correlate with the observed activity enhancement for oxygen surface exchange of the LSC_{214}-decorated LSC_{113} relative to LSC_{113}.

We here compare the relative change of the surface exchange coefficient (k^q) vs. the calculated O 2*p* band centers (relative to the Fermi level) between the LSC_{214}-decorated $LSCF_{113}$ (LSC_{113}) and the $LSCF_{113}$ (LSC_{113}) surfaces, as shown in Fig. 8a. We assign compositions utilizing the surface Sr content of the stable LSC_{113} and $LSCF_{113}$ (001) surfaces as well as the thermodynamic driving force of Sr_{La} substitution between LSC_{214} vs. LSC_{113} and LSC_{214} vs. $LSCF_{113}$. The calculated bulk O *2p* band centers (relative to the Fermi level) of $La_{1-x}Sr_xCoO_3$ and $(La_{1-x}Sr_x)_2CoO_4$ vs. the Sr concentration, *x*, are provided in the inlet plot of Fig. 8a, which indicates uplift of the O *2p* band centers (relative to the Fermi level) with increasing Sr. Based on the assumption that perovskite bulk O *2p* band centers can correlate with the surface defect and adsorption energetics as well as oxygen surface exchange activities,[54] an approximation was made to correlate the calculated bulk O *2p* centers calculated at assigned Sr content with the measured oxygen surface exchange activities. The LSC_{214} decoration on LSC_{113} leads to a highly Sr enriched top surface layer of LSC_{214} and LSC_{113} film[24] both with a higher O 2*p* band center than the LSC_{113} surface with lower Sr segregation (we use 62.5% Sr on the A site based on the COBRA measurement of LSC_{113} surface layer Sr concentration[75]). These higher 2*p* band centers lead to higher activities (~2 orders magnitude enhancement in k^q values). In contrast to the LSC_{113}, the stable $LSCF_{113}$ (001) surface is expected to have ~100% Sr from the DFT surface thermodynamic modeling , and negligible thermodynamic driving force for Sr_{La} interdiffusion

from the $LSCF_{113}$ to the LSC_{214} (Fig. 7). Consequently, there was no significant change on the O 2*p* band centers relative to the Fermi level with LSC_{214} decoration on $LSCF_{113}$, which is in agreement with the observed 2 fold enhancement of the k^q values of $LSCF_{113}$. Therefore, the distinct Sr occupancy changes within the LSC_{214}-on-$LSCF_{113}$ and LSC_{214}-on-LSC_{113} heterostructures may be responsible for the observed enhanced surface exchange kinetics relative to the undecorated $LSCF_{113}$ and LSC_{113} base films.

3.7 Stability of the $LSCF_{113}$, LSC_{113}, and LSC_{214} at full Sr substitution relative to decomposition

Previous COBRA studies[75] reveal that the top surface layer in the perovskite phase of LSC_{113} films may contain Sr concentration at 60% on the A site and detect that discrete particles epitaxially grown to the film surface can have $SrCoO_{3-\delta}$-like composition, in which particle surface might be covered by electrochemically inactive Sr-rich phases (such as SrO). It was hypothesized that the surface particles of $SrCoO_{3-\delta}$ are most likely to decompose to form secondary phases such as $SrO/Sr(OH)_2/SrCO_3$, which can greatly impede the surface exchange kinetics.[63, 78]

In analogy to the valence stability assessment of SOFC perovskites proposed by Yokokawa et al.,[72] in this section we evaluate stability of $LSCF_{113}$ and LSC_{113} surfaces without vs. with LSC_{214} decoration against surface degradation by investigating decomposition of fully Sr substituted $LSCF_{113}$, LSC_{113}, and LSC_{214} relative to the lower order binary oxides - SrO, Co_3O_4, Fe_2O_3, based on the surface Sr content reported in the COBRA measurements,[24, 59] and the reported surface chemical inhomogeneity, i.e. formation of SrO like particles.[55, 64] Although these reaction energies are calculated for bulk compositions, we will assume the give at least

qualitative guidance for the stability of the Sr enriched surface layers. As shown in Fig. 9a, the decomposition reaction free energy to form the lower order binary metal oxides - SrO, Co_3O_4, Fe_2O_3, which is equivalent to the negative formation free energy of $LSCF_{113}$, LSC_{113}, and LSC_{214} from the lower order binary metal oxides, are +0.443, +0.096, and +0.481 eV per formula unit at T = 550 °C and $p(O_2)$ = 1 atm, respectively. These values depend on the effective chemical potential of oxygen (see ESI† for more details of the definition on the effective chemical potential of oxygen for incorporation of temperature and $p(O_2)$ dependences in reaction free energies) and the computed *ab initio* formation energy of $SrCo_{0.25}Fe_{0.75}O_3$, $SrCoO_3$, and Sr_2CoO_4 (Table S1†). The positive reaction free energy means that an energy penalty is required to decompose the compound, and a larger value corresponds to a higher energy cost for the decomposition reaction and higher stability of the compound. Our *ab initio* decomposition reaction free energy results suggest that $SrCoO_3$ is more prone to decompose with respect to the lower order binary metal oxides than $SrCo_{0.25}Fe_{0.75}O_3$ and Sr_2CoO_4, while both $SrCo_{0.25}Fe_{0.75}O_3$ and Sr_2CoO_4 exhibit comparable stability against the decomposition at T = 550 °C and $p(O_2)$ = 1 atm.

In addition to the decomposition reaction relative to the binary metal oxides, it is also likely that decomposition of the perovskite may occur via the following reaction:[58, 76, 79]

$$SrCoO_3 \rightarrow \frac{1}{2}Sr_2CoO_4 + \frac{1}{6}Co_3O_4 + \frac{1}{6}O_2 \quad \text{.....(1)}$$

$$SrCo_{0.25}Fe_{0.75}O_3 \rightarrow \frac{1}{8}Sr_2CoO_4 + \frac{1}{24}Co_3O_4 + \frac{1}{24}O_2 + \frac{3}{4}SrFeO_3 \quad \text{.....(2)}$$

As shown in Fig. 9b, the calculated reaction free energies for the reaction (1) and (2) are -0.144

eV, and -0.019 eV (or +0.011 eV with the B-site configuration entropy term for $SrCo_{0.25}Fe_{0.75}O_3$), respectively, at T = 550 °C and $p(O_2)$ = 1 atm. Again, the decomposition with respect to Sr_2CoO_4 and Co_3O_4 formation is more exothermic for $SrCoO_3$ than $SrCo_{0.25}Fe_{0.75}O_3$, indicating a poorer stability of $SrCoO_3$ than $SrCo_{0.25}Fe_{0.75}O_3$ with respect to formation of Sr_2CoO_4 and Co_3O_4. It is also hypothesized that the Co_3O_4 formation in the reaction (1) and (2) may cause degradation of surface exchange activity, due to loss of the more active perovskite phase. Therefore, upon LSC_{214} decoration, both the reaction (1) and (2) will reduce the tendency to decompose (increasing activity of the reaction product can reduce the reaction driving force), while a much weaker reduction in the thermodynamic driving force is expected for $SrCo_{0.25}Fe_{0.75}O_3$ than $SrCoO_3$, as the decomposition reaction free energy of reaction (2) is close to 0 eV. It is noted that an additional B-site configuration entropy term for $SrCo_{0.25}Fe_{0.75}O_3$, which corresponds to ~-0.04 eV per formula unit, is neglected here, which will further stabilize $SrCo_{0.25}Fe_{0.75}O_3$ and not alter the stability trend discussed above.

In general, these results suggest, for the high Sr content we studied, that addition of Fe stabilizes the LSC_{113} phase and that the RP structures are more stable than the ABO_3 structures, at least for Co. Overall, the predicted stability trends of bulk $SrCo_{0.25}Fe_{0.75}O_3$, $SrCoO_3$, and Sr_2CoO_4 are in good agreement with the observed experimental trends of surface stability for $LSCF_{113}$, LSC_{113} with and without LSC_{214} decoration, suggesting a correlation between surface degradation/particle formation and stability differences among $LSCF_{113}$, LSC_{113}, and LSC_{214} against decomposition.

4. Conclusions

We show that LSC_{214} decoration on the (001)-oriented $LSCF_{113}$ thin films does not

greatly enhance the surface oxygen exchange kinetics in contrast to the heterostructured LSC_{214}-LSC_{113} surfaces, which has surface exchange coefficients up to ~2 orders of magnitude greater than LSC_{113}. In addition, the time-dependent degradation of the oxygen surface exchange kinetics of the LSC_{113} thin film is markedly improved by LSC_{214} decoration in contrast to the $LSCF_{113}$ with LSC_{214} coverage, where negligible changes are noted. AES reveals that the surface Sr concentration of the LSC_{113} significantly increases with LSC_{214} coverage, which is coupled with the suppression of the formation of secondary passive phases during annealing. In contrast, LSC_{214} decoration does not increase the surface Sr concentration of the $LSCF_{113}$. It is hypothesized that LSC_{214} decoration may be responsible for observed oxygen surface exchange kinetics and time-dependent surface stability, which is good agreement with the findings from DFT studies on the thermodynamic driving force for Sr migration from the $LSCF_{113}$ to LSC_{214} structure. *Ab* initio surface stability analysis shows that negligible increase in Sr concentration at the $LSCF_{113}$ (001) surface perovskite surfaces can be induced by LSC_{214} decoration as the AO-terminated surface has 100% SrO and there is little driving force for Sr to segregate to the $LSCF_{113}$ and LSC_{214} interface or into the LSC_{214} from the $LSCF_{113.}$ However, for the LSC_{113} (001) surface there is an opportunity for significant Sr enrichment, both because the LSC_{113} (001) surface has an unsaturated A-site Sr occupation and because there is a strong driving force for Sr to migrate from LSC_{113} to the interface with LSC_{214} and into the LSC_{214} phase itself. In addition, the calculated bulk decomposition reaction free energies of $SrCo_{0.25}Fe_{0.75}O_3$, $SrCoO_3$, and Sr_2CoO_4 with respect to the binary metal oxides or formation of the Sr_2CoO_4 and Co_3O_4 phases correlates with the observed experimental trend of surface stability $LSCF_{113}$, LSC_{113} with and without LSC_{214} decoration. This work shows that the influence of heterostructured interfaces on the oxygen surface exchange kinetics are highly dependent on the peroveskite surface and

surface stability, and detailed understanding on the interfacial chemistry is needed in order to use heterostructured interfaces to develop highly active and stable catalysts for oxygen electrocatalysis at elevated temperatures.

Associated Content

Electronic Supplementary Information (ESI†). Details about sample preparation, EIS testing, XRD, AFM, AES, and DFT. This material is available free of charge via the Internet

Acknowledgements

This work was supported by the Department of Energy (DOE), National Energy Technology Laboratory (NETL), Solid State Energy Conversion Alliance (SECA) Core Technology Program (Funding Opportunity Number DEFE0009435) and the Skoltech-MIT Center for Electrochemical Energy. The PLD and XRD performed were conducted at the Center for Nanophase Materials Sciences, which is sponsored at Oak Ridge National Laboratory by the Scientific User Facilities Division, Office of Basic Energy Sciences, U.S. Department of Energy, and computations in this work were also benefited from the use of the National Energy Research Scientific Computing Center allocation of the Center for Nanophase Materials Sciences at Oak Ridge National Laboratory, both under grant number CNMS2013-292.

Author Information

Corresponding Author:

* To whom correspondence should be addressed. ddmorgan@wisc.edu, shaohorn@mit.edu

Author Contributions:

[+] These authors contributed equally to this work.

References

1. Z. P. Shao and S. M. Haile, *Nature*, 2004, **431**, 170-173.
2. B. C. H. Steele and A. Heinzel, *Nature*, 2001, **414**, 345-352.
3. L. Yang, C. D. Zuo, S. Z. Wang, Z. Cheng and M. L. Liu, *Adv. Mater.*, 2008, **20**, 3280-3283.
4. L. da Conceicao, C. R. B. Silva, N. F. P. Ribeiro and M. Souza, *Mater. Charact.*, 2009, **60**, 1417-1423.
5. R. A. De Souza and J. A. Kilner, *Solid State Ion.*, 1998, **106**, 175-187.
6. R. A. De Souza and J. A. Kilner, *Solid State Ion.*, 1999, **126**, 153-161.
7. A. Endo, M. Ihara, H. Komiyama and K. Yamada, *Solid State Ion.*, 1996, **86-8**, 1191-1195.
8. T. Ioroi, T. Hara, Y. Uchimoto, Z. Ogumi and Z. Takehara, *J. Electrochem. Soc.*, 1997, **144**, 1362-1370.
9. S. B. Adler, *Solid State Ion.*, 1998, **111**, 125-134.
10. A. V. Berenov, A. Atkinson, J. A. Kilner, E. Bucher and W. Sitte, *Solid State Ion.*, 2010, **181**, 819-826.
11. T. Kawada, J. Suzuki, M. Sase, A. Kaimai, K. Yashiro, Y. Nigara, J. Mizusaki, K. Kawamura and H. Yugami, *J. Electrochem. Soc.*, 2002, **149**, E252-E259.

12. J. A. Kilner, R. A. DeSouza and I. C. Fullarton, *Solid State Ion.*, 1996, **86-8**, 703-709.

13. J. Mizusaki, Y. Mima, S. Yamauchi, K. Fueki and H. Tagawa, *J. Solid State Chem.*, 1989, **80**, 102-111.

14. V. G. Sathe, A. V. Pimpale, V. Siruguri and S. K. Paranjpe, *J. Phys.: Condens. Matter*, 1996, **8**, 3889-3896.

15. R. H. E. vanDoorn, I. C. Fullarton, R. A. deSouza, J. A. Kilner, H. J. M. Bouwmeester and A. J. Burggraaf, *Solid State Ion.*, 1997, **96**, 1-7.

16. J. M. Bae and B. C. H. Steele, *Solid State Ion.*, 1998, **106**, 247-253.

17. A. Esquirol, N. P. Brandon, J. A. Kilner and M. Mogensen, *J. Electrochem. Soc.*, 2004, **151**, A1847-A1855.

18. S. Hashimoto, Y. Fukuda, M. Kuhn, K. Sato, K. Yashiro and J. Mizusaki, *Solid State Ion.*, 2010, **181**, 1713-1719.

19. L. W. Tai, M. M. Nasrallah, H. U. Anderson, D. M. Sparlin and S. R. Sehlin, *Solid State Ion.*, 1995, **76**, 259-271.

20. L. W. Tai, M. M. Nasrallah, H. U. Anderson, D. M. Sparlin and S. R. Sehlin, *Solid State Ion.*, 1995, **76**, 273-283.

21. Y. Chen, Cai, Z., Kuru, Y., Ma, W., Tuller, H. L. and Yildiz, B., *Adv. Energy Mater.*, 2013, **3**, 1221–1229.

22. E. J. Crumlin, E. Mutoro, S. J. Ahn, G. J. la O, D. N. Leonard, A. Borisevich, M. D. Biegalski, H. M. Christen and Y. Shao-Horn, *J. Phys. Chem. Lett.*, 2010, **1**, 3149-3155.

23. Z. Feng, E. J. Crumlin, W. T. Hong, D. Lee, E. Mutoro, M. D. Biegalski, H. Zhou, H. Bluhm, H. M. Christen and Y. Shao-Horn, *J. Phys. Chem. Lett.*, 2013, **4**, 1512-1518.

24. Z. X. Feng, Y. Yacoby, M. J. Gadre, Y. L. Lee, W. T. Hong, H. Zhou, M. D. Biegalski,

H. M. Christen, S. B. Adler, D. Morgan and Y. Shao-Horn, *J. Phys. Chem. Lett.*, 2014, **5**, 1027-1034.

25. M. J. Gadre, Y. L. Lee and D. Morgan, *Phys. Chem. Chem. Phys.*, 2012, **14**, 2606-2616.

26. J. W. Han and B. Yildiz, *Energy Environ. Sci.*, 2012, **5**, 8598-8607.

27. D. Lee, Y.-L. Lee, A. Grimaud, W. T. Hong, M. D. Biegalski, D. Morgan and Y. Shao-Horn, *J. Phys. Chem. C*, 2014, **118**, 14326-14334.

28. M. Sase, F. Hermes, T. Nakamura, K. Yashiro, K. Sato, J. Mizusaki, T. Kawada, N. Sakai, K. Yamaji, T. Horita and H. Yokokawa, in *Solid Oxide Fuel Cells 10*, eds. K. Eguchi, S. C. Singhai, H. Yokokawa and H. Mizusaki, Electrochemical Society Inc, Pennington, 2007, vol. 7, pp. 1055-1060.

29. M. Sase, F. Hermes, K. Yashiro, K. Sato, J. Mizusaki, T. Kawada, N. Sakai and H. Yokokawa, *J. Electrochem. Soc.*, 2008, **155**, B793-B797.

30. M. Sase, K. Yashiro, K. Sato, J. Mizusaki, T. Kawada, N. Sakai, K. Yamaji, T. Horita and H. Yokokawa, *Solid State Ion.*, 2008, **178**, 1843-1852.

31. A. Unemoto, K. Nagao, T. Tairako, K. Amezawa and T. Kawada, in *Ionic and Mixed Conducting Ceramics 7*, eds. M. Mogensen, T. Armstrong, T. M. Gur and H. Yokokawa, Electrochemical Soc Inc, Pennington, 2010, vol. 28, pp. 59-70.

32. K. Yashiro, T. Nakamura, M. Sase, F. Hermes, K. Sato, T. Kawada and J. Mizusaki, in *Solid Oxide Fuel Cells 10*, eds. K. Eguchi, S. C. Singhai, H. Yokokawa and H. Mizusaki, Electrochemical Society Inc, Pennington, 2007, vol. 7, pp. 1287-1292.

33. K. Yashiro, T. Nakamura, M. Sase, F. Hermes, K. Sato, T. Kawada and J. Mizusaki, *Electrochem. Solid State Lett.*, 2009, **12**, B135-B137.

34. E. J. Crumlin, E. Mutoro, W. T. Hong, M. D. Biegalski, H. M. Christen, Z. Liu, H.

Bluhm and Y. Shao-Horn, *J. Phys. Chem. C*, 2013, **117**, 16087-16094.

35. A. Mitterdorfer and L. J. Gauckler, *Solid State Ion.*, 1998, **111**, 185-218.

36. G. Kresse and J. Hafner, *Phys. Rev. B*, 1993, **47**, 558.

37. G. Kresse and J. Furthmuller, *Phys. Rev. B*, 1996, **54**, 11169-11186.

38. P. E. Blochl, *Phys. Rev. B*, 1994, **50**, 17953-17979.

39. J. P. Perdew and Y. Wang, *Phys. Rev. B*, 1992, **45**, 13244.

40. V. I. Anisimov, F. Aryasetiawan and A. I. Lichtenstein, *J. Phys.: Condens. Matter*, 1997, **9**, 767-808.

41. S. L. Dudarev, G. A. Botton, S. Y. Savrasov, C. J. Humphreys and A. P. Sutton, *Phys. Rev. B*, 1998, **57**, 1505-1509.

42. Y.-L. Lee, J. Kleis, J. Rossmeisl and D. Morgan, *Phys. Rev. B: Condens. Matter Mater. Phys.*, 2009, **80**, 224101.

43. C. Tealdi, C. Ferrara, L. Malavasi, P. Mustarelli, C. Ritter, G. Chiodelli and Y. A. Diaz-Fernandez, *Phys. Rev. B*, 2010, **82**, 8.

44. D. Lee, A. Grimaud, E. J. Crumlin, K. Mezghani, M. A. Habib, Z. X. Feng, W. T. Hong, M. D. Biegalski, H. M. Christen and Y. Shao-Horn, *J. Phys. Chem. C*, 2013, **117**, 18789-18795.

45. D. Lee, Y.-L. Lee, A. Grimaud, W. T. Hong, M. D. Biegalski, D. Morgan and Y. Shao-Horn, *J. Mater. Chem. A*, 2014, **2**, 6480-6487.

46. E. J. Crumlin, S. J. Ahn, D. Lee, E. Mutoro, M. D. Biegalski, H. M. Christen and Y. Shao-Horn, *J. Electrochem. Soc.*, 2012, **159**, F219-F225.

47. M. James, A. Tedesco, D. Cassidy, M. Colella and P. J. Smythe, *J. Alloy. Compd.*, 2006, **419**, 201-207.

48. R. H. E. van Doorn and A. J. Burggraaf, *Solid State Ion.*, 2000, **128**, 65-78.

49. S. B. Adler, *Chem. Rev.*, 2004, **104**, 4791-4843.

50. B. C. H. Steele and J. M. Bae, *Solid State Ion.*, 1998, **106**, 255-261.

51. F. S. Baumann, J. Fleig, H. U. Habermeier and J. Maier, *Solid State Ion.*, 2006, **177**, 1071-1081.

52. C. R. Kreller, T. J. McDonald, S. B. Adler, E. J. Crumlin, E. Mutoro, S. J. Ahn, G. J. la O, Y. Shao-Horn, M. D. Biegalski, H. M. Christen, R. R. Chater and J. A. Kilner, *J. Electrochem. Soc.*, 2013, **160**, F931-F942.

53. G. J. la O, S. J. Ahn, E. Crumlin, Y. Orikasa, M. D. Biegalski, H. M. Christen and Y. Shao-Horn, *Angew. Chem.-Int. Edit.*, 2010, **49**, 5344-5347.

54. Y. L. Lee, J. Kleis, J. Rossmeisl, Y. Shao-Horn and D. Morgan, *Energy Environ. Sci.*, 2011, **4**, 3966-3970.

55. M. Kubicek, A. Limbeck, T. Fromling, H. Hutter and J. Fleig, *J. Electrochem. Soc.*, 2011, **158**, B727-B734.

56. E. J. Crumlin, E. Mutoro, Z. Liu, M. E. Grass, M. D. Biegalski, Y. L. Lee, D. Morgan, H. M. Christen, H. Bluhm and Y. Shao-Horn, *Energy Environ. Sci.*, 2012, **5**, 6081-6088.

57. E. Mutoro, E. J. Crumlin, H. Pöpke, B. Luerssen, M. Amati, M. K. Abyaneh, M. D. Biegalski, H. M. Christen, L. Gregoratti, J. Janek and Y. Shao-Horn, *J. Phys. Chem. Lett.*, 2011, **3**, 40-44.

58. J. Ovenstone, J. S. White and S. T. Misture, *J. Power Sources*, 2008, **181**, 56-61.

59. Z. Feng, Y. Yacoby, W. T. Hong, H. Zhou, M. D. Biegalski, H. M. Christen and Y. Shao-Horn, *Energy Environ. Sci.*, 2014, **7**, 1166-1174.

60. H. M. Reichenbach and P. J. McGinn, *Appl. Catal. A-Gen.*, 2003, **244**, 101-114.

61. L. Karvonen, S. H. Yoon, P. Hug, H. Yamauchi, A. Weidenkaff and M. Karppinen, *Mater. Res. Bull.*, 2011, **46**, 1340-1345.

62. A. N. Petrov, V. A. Cherepanov, O. F. Kononchuk and L. Y. Gavrilova, *J. Solid State Chem.*, 1990, **87**, 69-76.

63. E. Fischer, W. D. Shen and J. L. Hertz, *J. Electroceram.*, 2012, **29**, 262-269.

64. D. Oh, D. Gostovic and E. D. Wachsman, *J. Mater. Res.*, 2012, **27**, 1992-1999.

65. Z. H. Cai, M. Kubicek, J. Fleig and B. Yildiz, *Chem. Mat.*, 2012, **24**, 1116-1127.

66. H. Huhtinen, J. Järvinen, R. Laiho, P. Paturi and J. Raittila, *J. Appl. Phys*, 2001, **90**, 1521-1528.

67. T. Nitadori, M. Muramatsu and M. Misono, *Chem. Mat.*, 1989, **1**, 215-220.

68. H. P. Ding, A. V. Virkar, M. L. Liu and F. Liu, *Phys. Chem. Chem. Phys.*, 2013, **15**, 489-496.

69. J. Druce, H. Tellez, M. Burriel, M. D. Sharp, L. J. Fawcett, S. N. Cook, D. S. McPhail, T. Ishihara, H. H. Brongersma and J. A. Kilner, *Energy Environ. Sci.*, 2014, **7**, 3593-3599.

70. K. Szot and W. Speier, *Phys. Rev. B*, 1999, **60**, 5909-5926.

71. W. Lee, J. W. Han, Y. Chen, Z. H. Cai and B. Yildiz, *J. Am. Chem. Soc.*, 2013, **135**, 7909-7925.

72. H. Yokokawa, N. Sakai, T. Horita, K. Yamaji, M. E. Brito and H. Kishimoto, *J. Alloy. Compd.*, 2008, **452**, 41-47.

73. J. Druce, T. Ishihara and J. Kilner, *Solid State Ion.*, 2014, **262**, 893-896.

74. M. Burriel, G. Garcia, J. Santiso, J. A. Kilner, J. C. C. Richard and S. J. Skinner, *J. Mater. Chem.*, 2008, **18**, 416-422.

75. Z. Feng, Y. Yacoby, W. Hong, H. Zhou, M. Biegalski, H. Christen and Y. Shao-Horn,

Energy Environ. Sci., 2014, **7**, 1166-1174.

76. J. Hayd, H. Yokokawa and E. Ivers-Tiffee, *J. Electrochem. Soc.*, 2013, **160**, F351-F359.

77. A. Grimaud, K. J. May, C. E. Carlton, Y. L. Lee, M. Risch, W. T. Hong, J. Zhou and Y. Shao-Horn, *Nat. Commun.*, 2013, **4**, 2439.

78. V. V. Vashook, M. V. Zinkevich, H. Ullmann, J. Paulsen, N. Trofimenko and K. Teske, *Solid State Ion.*, 1997, **99**, 23-32.

79. F. Morin, G. Trudel and Y. Denos, *Solid State Ion.*, 1997, **96**, 129-139.

Table of Content (max: 3.14" x 1.57")

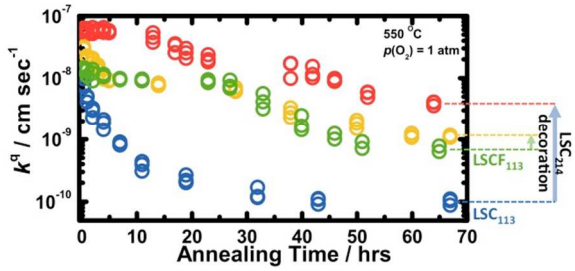

The effect of $(La_{0.5}Sr_{0.5})CoO_{4\pm\delta}$ decoration on the time-dependent surface exchange coefficient (k^q) of the epitaxial $La_{0.8}Sr_{0.2}CoO_{3-\delta}$ and $La_{0.6}Sr_{0.4}Co_{0.2}Fe_{0.8}O_{3-\delta}$ thin films.

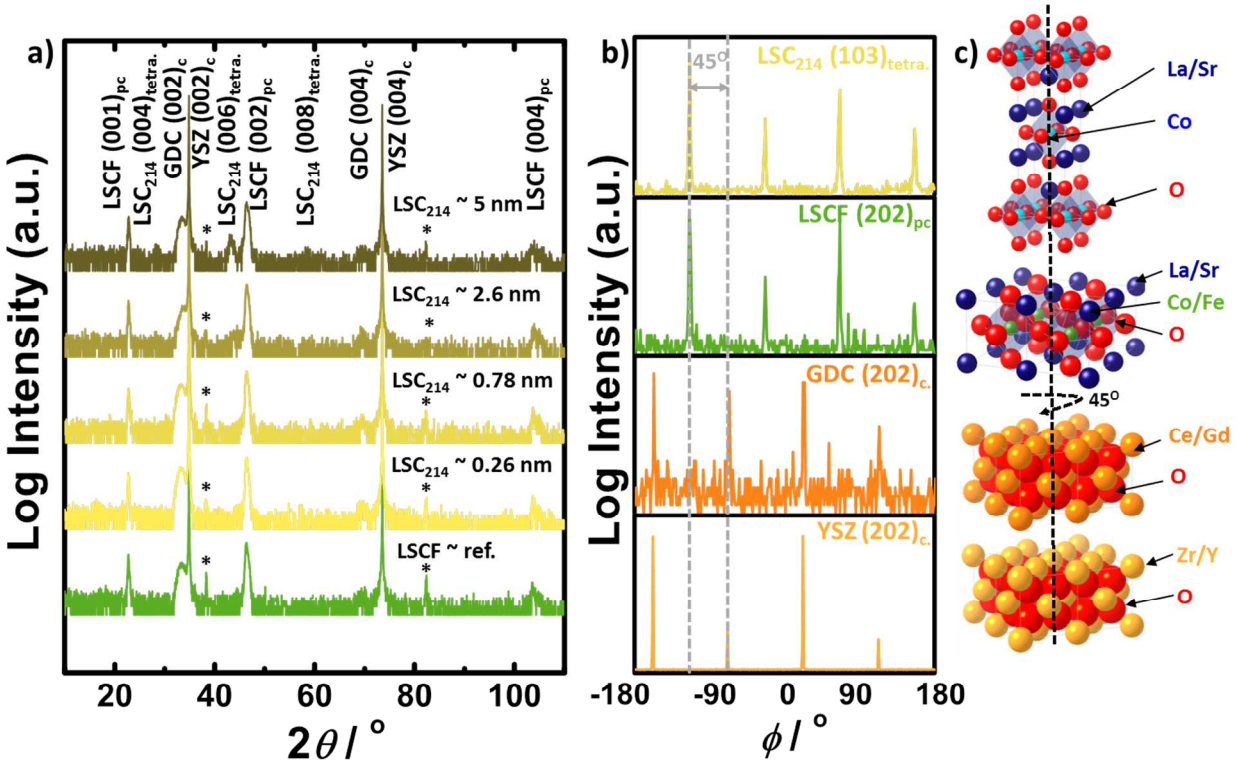

Fig. 1. X-ray diffraction (Cu K_α) analysis at room temperature. (a) Normal XRD of the epitaxial $LSCF_{113}$ reference and the LSC_{214}-decorated $LSCF_{113}$ films, (b) off-normal XRD of a similarly prepared sample with a thicker (~5 nm) LSC_{214} coverage, and (c) schematic of the crystallographic rotational relationships among the $LSC_{214}(001)_{tetra.}$, $LSCF_{113}(001)_{pc}$, $GDC(001)_{cubic}$, and $YSZ(001)_{cubic}$.

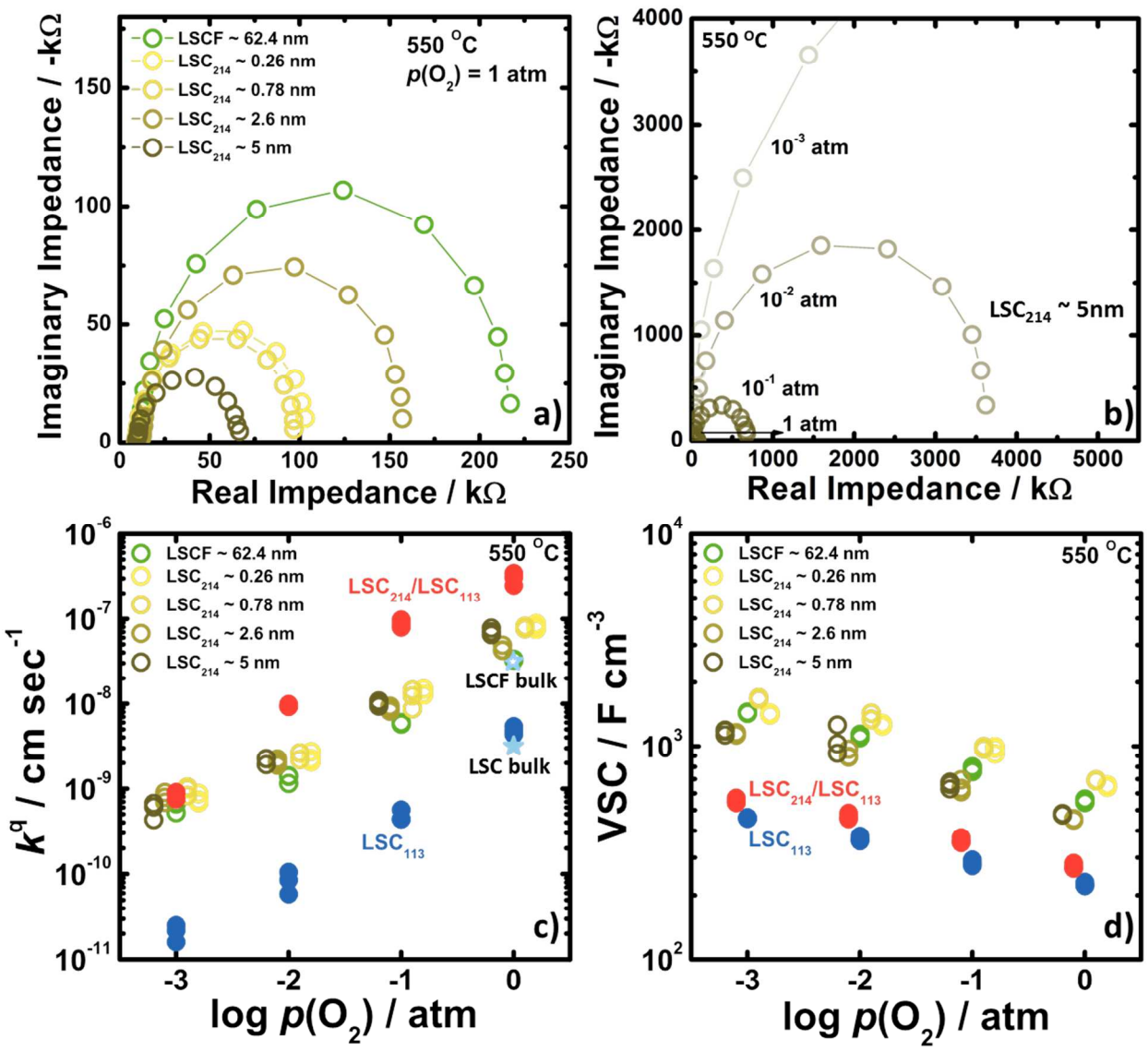

Fig. 2. Electrochemical impedance spectroscopy (EIS) results of microelectrodes (~200 μm) for the bare $LSCF_{113}$ film, LSC_{113} film, $LSCF_{113}$ films with ~0.3, ~0.8, ~2.6, and ~5 nm LSC_{214} decorations, LSC_{113} film with ~2.6 nm LSC_{214} decoration at 550 ºC. (a) Nyquist plot of the epitaxial $LSCF_{113}$ and the epitaxial LSC_{214}-decorated $LSCF_{113}$ films in 1 atm. (b) Nyquist plot of the $LSCF_{113}$ thin film with ~5 nm LSC_{214} coverage as a function of $p(O_2)$. (c) Oxygen partial pressure dependency of the surface exchange coefficients (k^q) of the $LSCF_{113}$, LSC_{113}, LSC_{214}-decorated $LSCF_{113}$, LSC_{214}-decorated LSC_{113} films calculated from EIS spectra collected at 550

ºC. Extrapolated bulk k^* (approximately equivalent to k^q) values at 550 ºC obstained from previous data of (☆-light blue) Steele et al.[50] and (★-light blue) De souza et al.[6] are plotted for comparison. (d) Oxygen partial pressure dependency of volume specific capacitance (*VSC*) of the epitaxial $LSCF_{113}$, LSC_{113}, LSC_{214}-decorated $LSCF_{113}$, and LSC_{214}-decorated LSC_{113} films calculated from EIS spectra collected at 550 ºC.

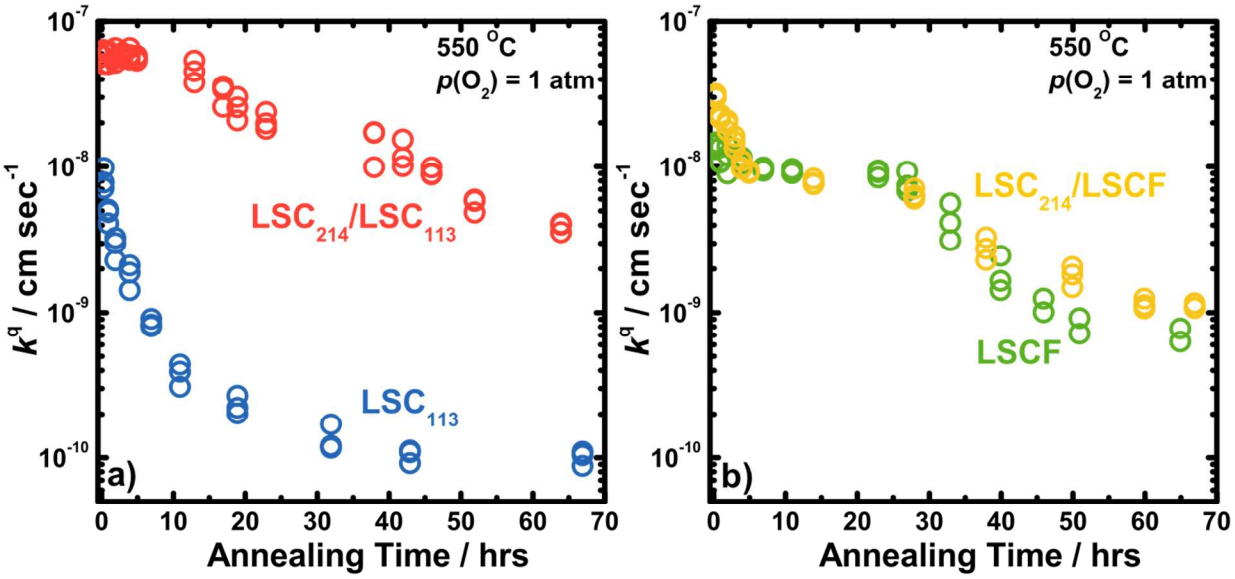

Fig. 3. Surface exchange coefficient (k^q) of microelectrodes (~200 μm) for (a) the LSC_{113} with and without LSC_{214} coverage and (b) the $LSCF_{113}$ with and without LSC_{214} coverage as a function of annealing time. Annealing was performed at 550 ºC in an oxygen partial pressure of 1 atm. Three microelectrodes from each sample were measured at the same annealing time.

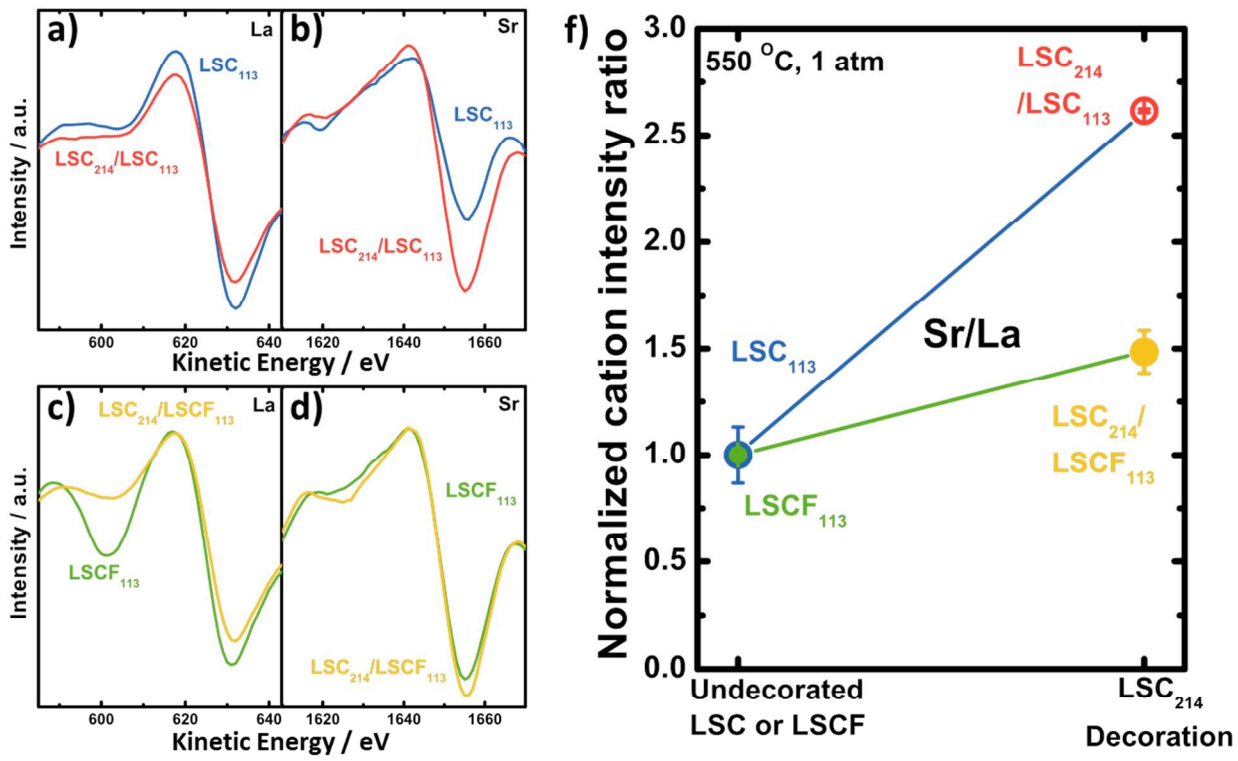

Fig. 4. Auger electron spectroscopy (AES) data from area mode for the $LSCF_{113}$ (green), LSC_{113} (blue), $LSCF_{113}$ film with ~2.6 nm LSC_{214} decorations (yellow), and LSC_{113} film with ~2.6 nm LSC_{214} decoration (red) after annealing. Annealing was performed at 550 ºC for 6 hours in an oxygen partial pressure of 1 atm. (a) La Auger spectra and (b) Sr Auger spectra of the LSC_{113} and LSC_{214}-decorated LSC_{113} films. (c) La Auger spectra and (d) Sr Auger spectra of the $LSCF_{113}$ and LSC_{214}-decorated $LSCF_{113}$ films. (f) Normalized La and Sr intensity ratio extracted from AES of the $LSCF_{113}$ films with and without ~2.6 nm LSC_{214} decorations, and LSC_{113} film with and without ~2.6 nm LSC_{214} decoration. Details of normalization methods are provided in the ESI †.

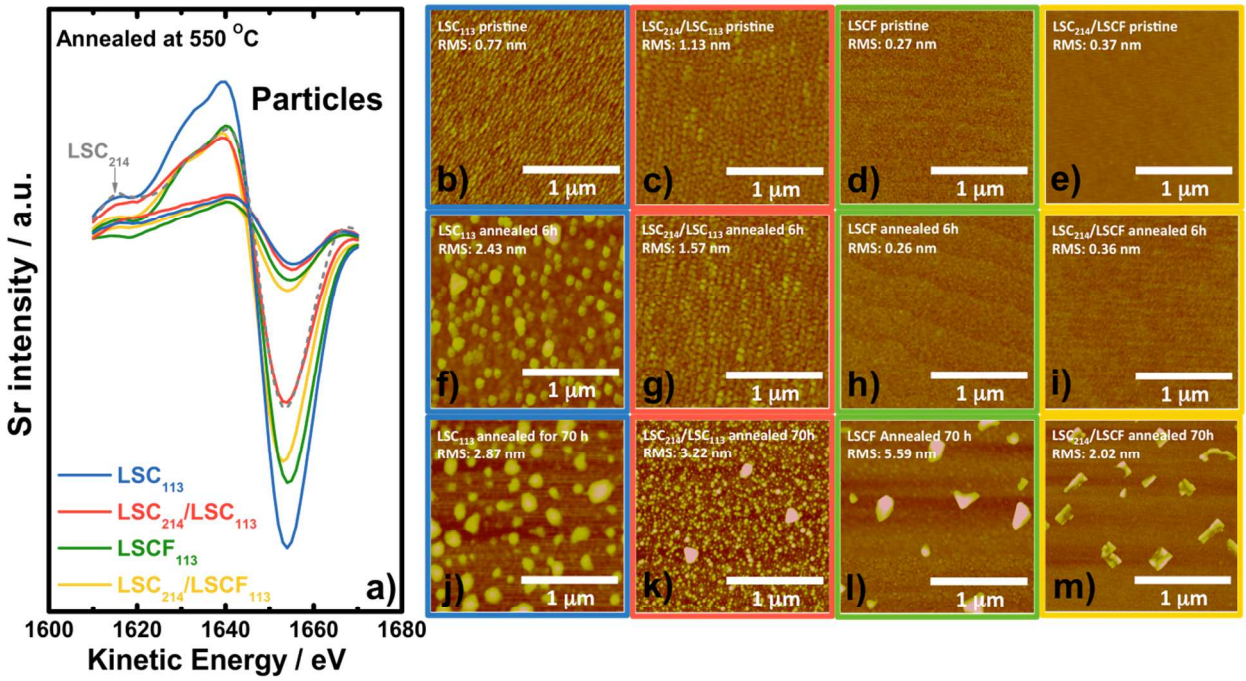

Fig. 5. Auger spectra and atomic force microscopy (AFM) images for bare LSC_{113}, $LSCF_{113}$, LSC_{214}-decorated LSC_{113}, and LSC_{214}-decorated $LSCF_{113}$ thin films. (a) Sr Auger spectra for: LSC_{113} (blue), LSC_{214}-decorated LSC_{113} (red), $LSCF_{113}$ (green), and LSC_{214}-decorated $LSCF_{113}$ (yellow) after annealing at 550 ^{O}C for 70 hours in an oxygen pressure of 1 atm. The dashed gray line is the Sr spectra of a pristine LSC_{214} reference sample. The peak-to-peak values in Auger spectra reflect the Sr concentrations. AFM images of as-deposited (b) LSC_{113}, (c) LSC_{214}-decorated LSC_{113}, (d) $LSCF_{113}$, and (e) LSC_{214}-decorated $LSCF_{113}$. AFM image showed particle formation on (f) 6 h annealed LSC_{113} but no particles were observed on (g) 6 h annealed LSC_{214}-decorated LSC_{113}, (h) 6 h annealed LSC_{214}-decorated LSC_{113}, and (i) 6 h annealed LSC_{214}-decorated LSC_{113}. After annealing for 70 h, particles were observed on all surfaces; (j) annealed LSC_{113}, (k) annealed LSC_{214}-decorated LSC_{113} (l) annealed $LSCF_{113}$ and (m) annealed LSC_{214}-decorated $LSCF_{113}$.

(a)

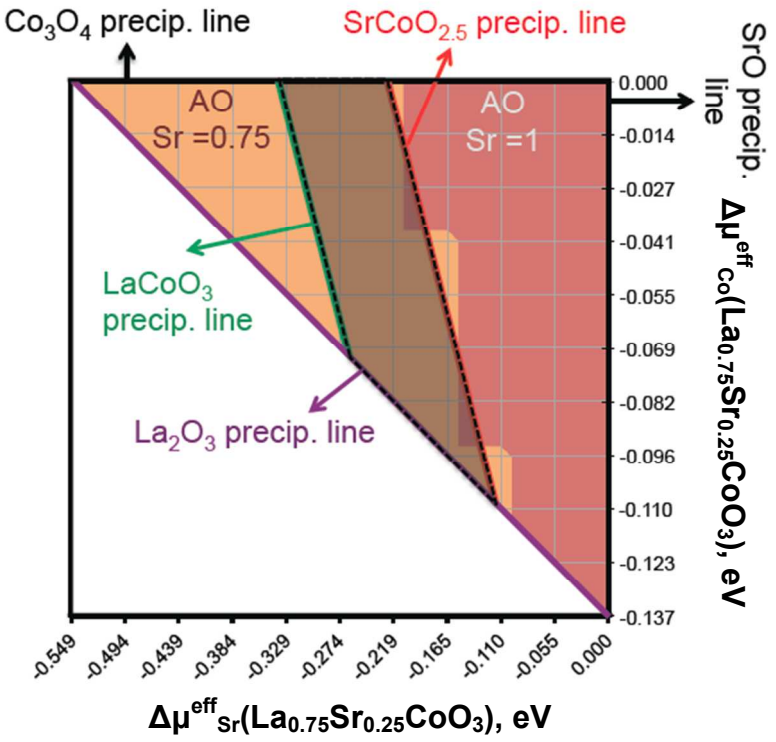

(b)

$\Delta\mu^{eff}_{Fe}(La_{0.625}Sr_{0.375}Fe_{0.75}Co_{0.25}O_3)$ = -0.12 eV vs. μ^{eff}_{Fe} (Fe_2O_3)

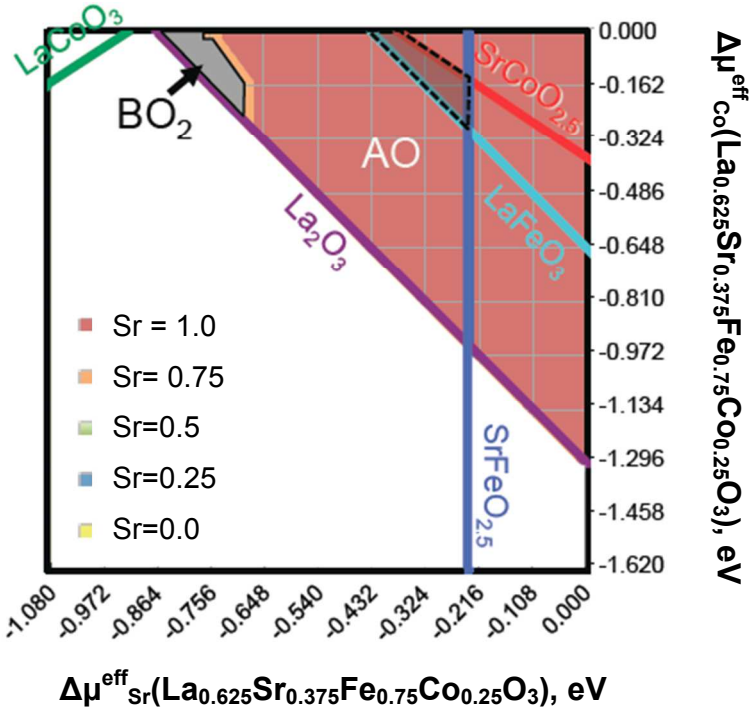

(c)

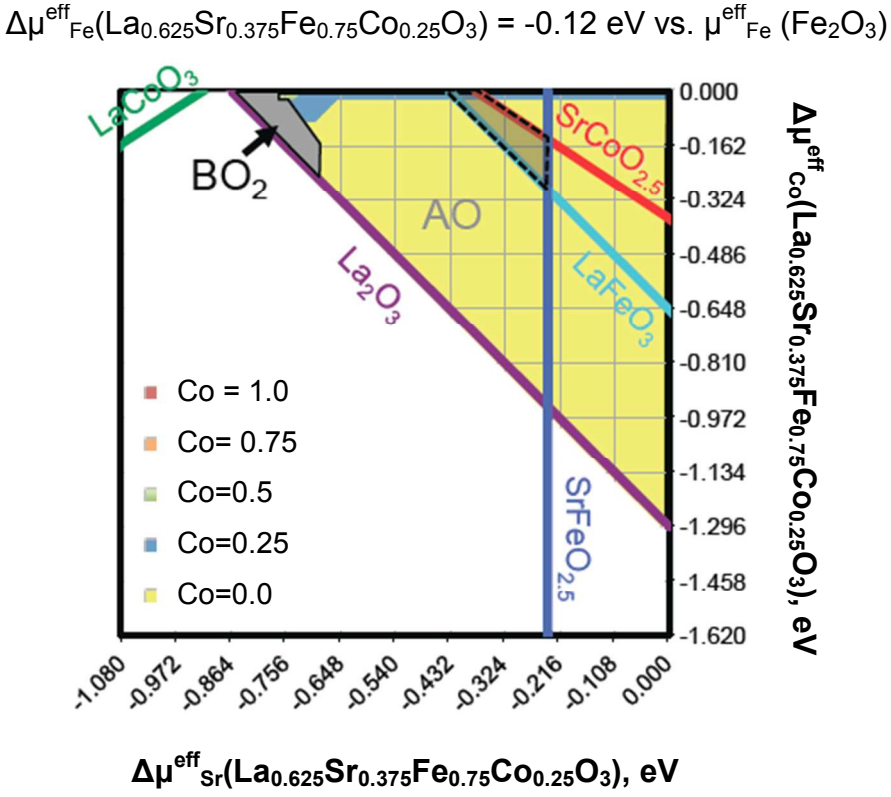

(d)

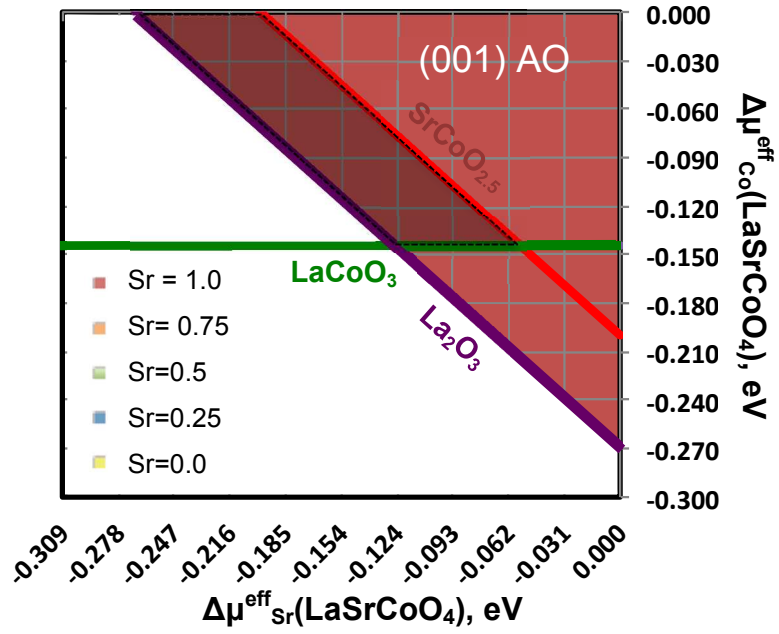

Fig. 6. Fig. 6a is the predicted $La_{0.75}Sr_{0.25}CoO_3$ surface stability diagram at T = 550 °C and $p(O_2)$ = 1 atm based on the effective metal chemical potentials of bulk $La_{0.75}Sr_{0.25}CoO_3$. The grid points

represent the sampled bulk effective chemical potentials of Sr (x-axis; x=0 represents the equilibrium between $La_{0.75}Sr_{0.25}CoO_3$ and SrO) and Co (y-axis; y=0 represents the equilibrium between $La_{0.75}Sr_{0.25}CoO_3$ and Co_3O_4) in $La_{0.75}Sr_{0.25}CoO_3$, and the contour plot beyond the grid is constructed based on the calculated lowest surface energy among the investigated $La_{0.75}Sr_{0.25}CoO_3$ (001) surface configurations. The shaded area within dotted lines represents the $La_{0.75}Sr_{0.25}CoO_3$ bulk stable region relative to the lower order oxide compounds ($LaCoO_3$–green, $SrCoO_{2.5}$–red, La_2O_3–purple, SrO–x=0, and Co_3O_4–y=0), the surface energy results are provided in Table S2†. The $La_{0.75}Sr_{0.25}CoO_3$ (001) surface stability analysis results suggest the most stable surfaces are the AO surfaces with the surface layer A-site Sr concentration equal to 0.75 within the bulk stable region relative to the lower order oxide compounds. Fig. 6b and c are the predicted $La_{0.625}Sr_{0.375}Fe_{0.75}Co_{0.25}O_3$ (001) top two surface layer Sr and Co composition at T = 550 °C and $p(O_2)$ = 1 atm at the condition of $\Delta\mu^{eff}_{Fe}(La_{0.625}Sr_{0.375}Fe_{0.75}Co_{0.25}O_3)$ = -0.12 eV vs. μ^{eff}_{Fe} (Fe_2O_3). The grid points represent the sampled bulk effective chemical potentials of Sr (x-axis; x=0 represents the equilibrium between $La_{0.625}Sr_{0.375}Fe_{0.75}Co_{0.25}O_3$ and SrO) and Co (y-axis; y=0 represents the equilibrium between $La_{0.625}Sr_{0.375}Fe_{0.75}Co_{0.25}O_3$ and Co_3O_4) in $La_{0.625}Sr_{0.375}Fe_{0.75}Co_{0.25}O_3$. The effective chemical potential conditions in which the BO_2 surface is more stable than the AO are presented by the grey area. The shaded area within dotted lines in Fig. 6b and 6c represents the $La_{0.625}Sr_{0.375}Fe_{0.75}Co_{0.25}O_3$ bulk stable region relative to the lower order oxides ($LaFeO_3$–light blue, $SrFeO_{2.5}$–deep blue, $LaCoO_3$–green, $SrCoO_{2.5}$–red, La_2O_3–purple, SrO–x=0, and Co_3O_4–y=0). The $La_{0.625}Sr_{0.375}Fe_{0.75}Co_{0.25}O_3$ (001) surface stability analysis results suggest the most stable surfaces are the AO surfaces with the surface layer A-site Sr concentration equal to 1.00 and such conclusion holds for all the other investigated conditions of $\Delta\mu^{eff}_{Fe}(La_{0.625}Sr_{0.375}Fe_{0.75}Co_{0.25}O_3)$, including $\Delta\mu^{eff}_{Fe}(La_{0.625}Sr_{0.375}Fe_{0.75}Co_{0.25}O_3)$ = 0.0, -0.24, -

0.36 eV vs. μ^{eff}_{Fe} (Fe_2O_3), as shown in Fig. S13a†, S13c†, and S13d†. Fig. 6d is the predicted contour plots for the $LaSrCoO_4$ stable (001) vs. (100) surface layer compositions within the bulk $LaSrCoO_4$ stability boundaries (in equilibrium with La_2O_3, SrO, Co_3O_4, $LaCoO_3$, and $SrCoO_{2.5}$) based on the most stable surface energy of the investigated six $LaSrCoO_4$ (001) and (100) slab configurations (see Fig. S11† for more details) vs. chemical potentials of Sr (relative to SrO) and Co (relative to Co_3O_4) at T = 550 °C and $p(O_2)$ = 1 atm. The shaded region represents the stable bulk $LaSrCoO_4$. For the same surface orientation, both the (001) AO and the (100) A_2BO_4 surfaces are predicted to be stable with fully enriched surface layer Sr at the A-sites. Comparatively, the surface energy of the fully Sr-enriched (100) A_2BO_4 surface is found to be a factor of 1.2 ~ 2 with respect to the surface energy of the fully Sr-enriched (001) AO surface within the stable bulk $LaSrCoO_4$ region, suggesting the greater stability of the (001) AO surface with fully enriched Sr vs. the (100) A_2BO_4 surfaces. Details of the *ab initio* thermodynamic analysis, definition of the effective chemical potentials, and additional information regarding to the sub-surface layer B-site composition, are provided in the ESI†.

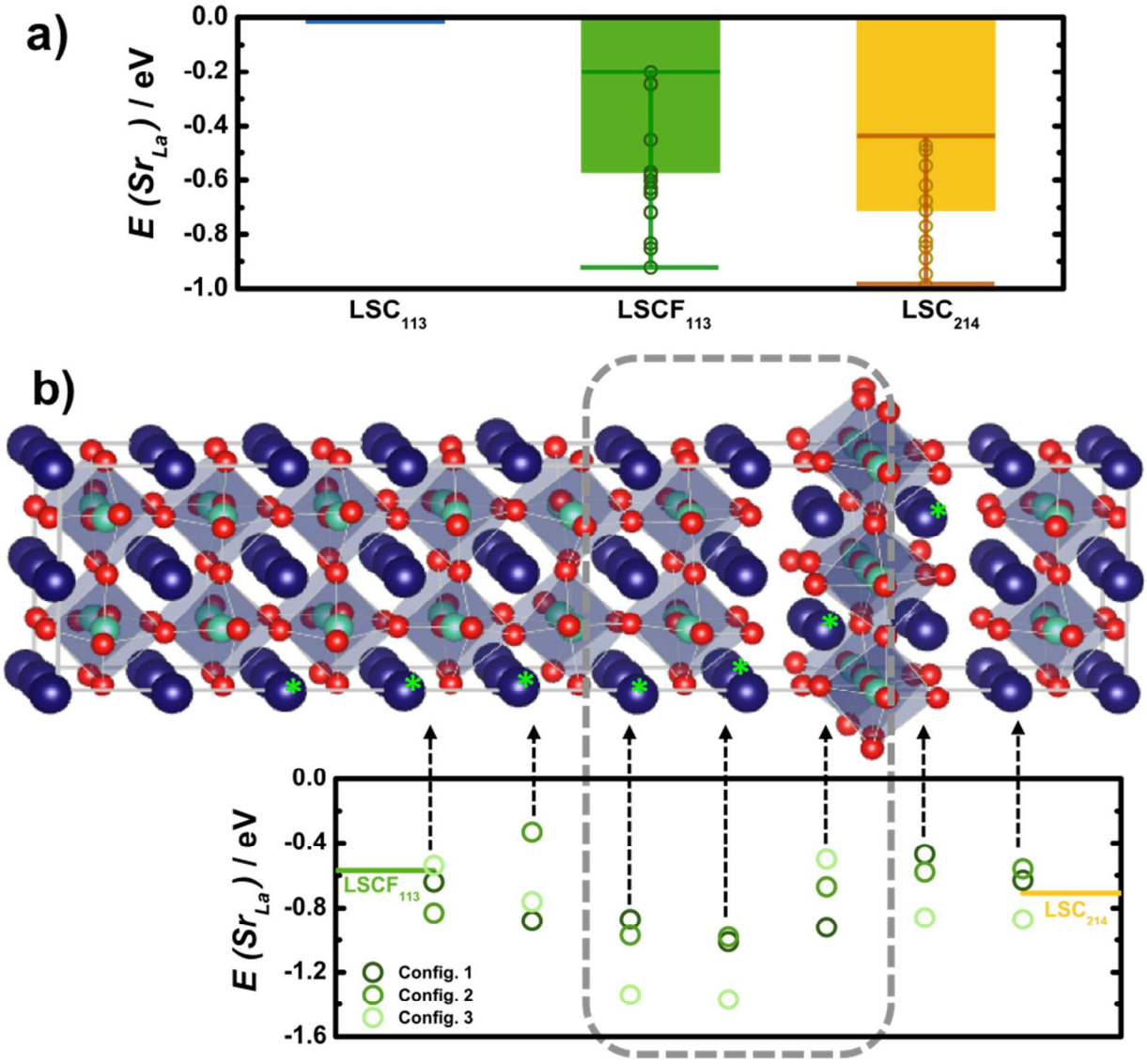

Fig. 7. (a) The calculated Sr_{La} substitution energies in bulk LSC_{214}, LSC_{113}, and $LSCF_{113}$ (all relative to that of LSC_{113}, which is set to 0). The error bars shown in the $LSCF_{113}$ and LSC_{214} represent the upper bound and lower bound of the Sr_{La} substitution energies from the sampled A-site and B-site cation arrangements, and the values are calculated based on the difference in the calculated total energies between a $La_{0.625}Sr_{0.375}CoO_3$ ($La_{0.5}Sr_{0.5}Fe_{0.75}Co_{0.25}O_3$) bulk and a $La_{0.75}Sr_{0.25}CoO_3$ ($La_{0.625}Sr_{0.375}Fe_{0.75}Co_{0.25}O_3$) bulk. Similarly, the Sr_{La} substitution energy for LSC_{214} was calculated using the total energy difference between LSC_{214} and

($La_{0.4375}Sr_{0.5625})_2CoO_4$). (b) The heterostructured interface model used in the DFT simulations and the results of Sr_{La} substitution energies. Elements are represented as: La/Sr (dark blue), Fe/Co (light blue, center of the octahedra), and O (red). The dashed rounded rectangle represents an interfacial region. The relative stability of Sr_{La} substitution energy relative to $La_{0.75}Sr_{0.25}CoO_3$, or E(Sr_{La}) of heterointerface - E(Sr_{La}) of LSC_{113}(25%Sr), is shown for the Sr_{La} substitution position in different AO planes labeled with asterisk(*). Values are relative to a bulk LSC_{113}(25%Sr) reference (y=0). Also shown is a yellow horizontal line representing the Sr_{La} substitution energies for the bulk $LSCF_{113}$ (E(Sr_{La}) of $LSCF_{113}$ - E(Sr_{La}) of LSC_{113}(25%Sr)), and a orange line for the bulk LSC_{214} (or E(Sr_{La}) of LSC_{214} - E(Sr_{La}) of LSC_{113}(25%Sr)). Note that the more negative values on the y-axis correspond to the easier substitution of the Sr_{La} relative to bulk LSC_{113}(25%Sr), and three A-site and B-site cation arrangements in the heterostructured interface models are explored to calculate the Sr_{La} substitution energy relative to $La_{0.75}Sr_{0.25}CoO_3$ (See Fig. S9† for more details on the DFT modeling).

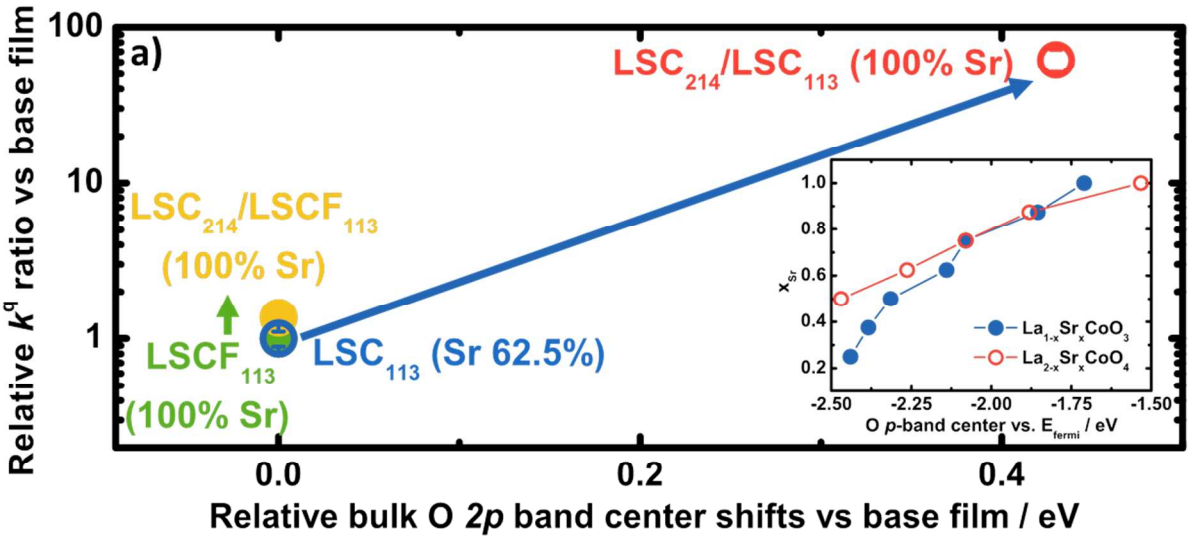

Fig. 8. (a) The relative ratio of the surface exchange coefficient k^q (with respect to the k^q of the base film) vs. the calculated bulk O 2*p* band center shifts (relative to the Fermi level) between the LSC_{214}-decorated $LSCF_{113}$ (LSC_{113}) film surfaces and the undecorated $LSCF_{113}$ (LSC_{113}) film surfaces based on the surface Sr information from COBRA analysis[63] and DFT modeling predictions. The inset shows the Sr content vs the calculated bulk O 2*p* band centers of LSC_{113} and LSC_{214}.

(a)

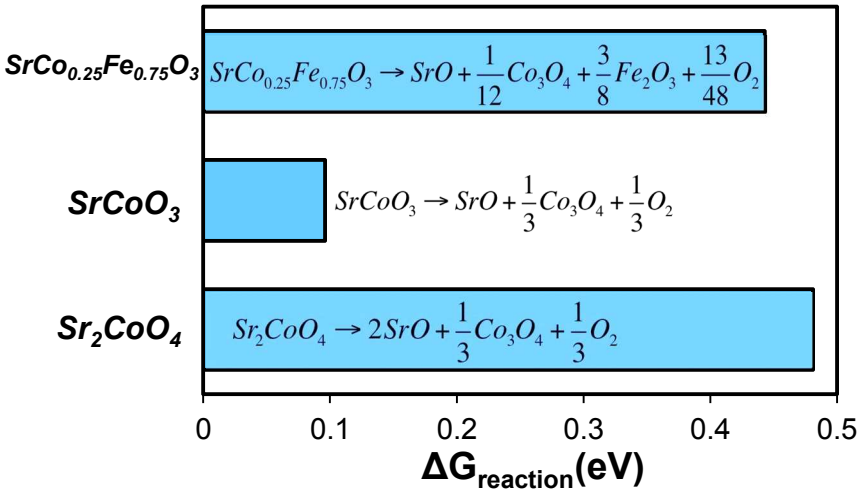

(b)

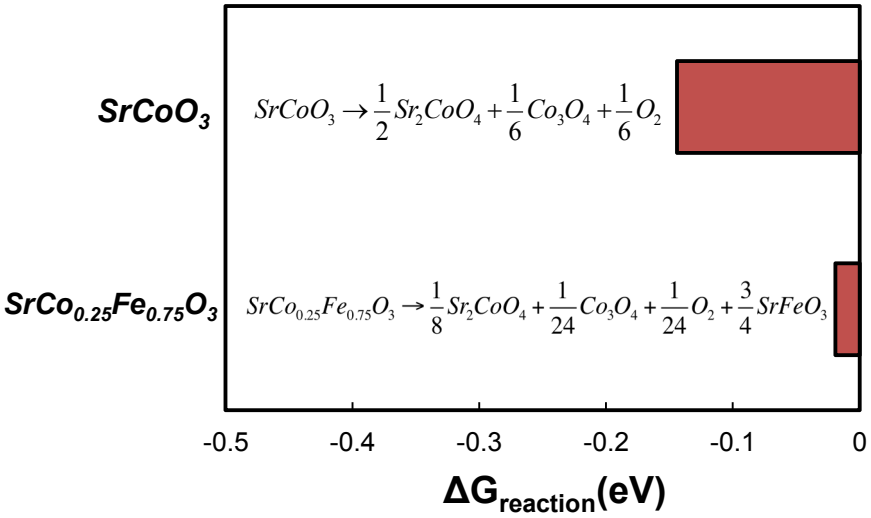

Fig. 9. (a) The decomposition reaction free energy to form the lower order binary metal oxides of fully Sr enriched $LSCF_{113}$, LSC_{113}, and LSC_{214}. (b) The decomposition reaction free energy to form Sr_2CoO_4 and lower order transition metal binary metal oxides of fully Sr enriched LSC_{113} and $LSCF_{113}$, both at T = 550 °C and $p(O_2)$ = 1 atm. We note that an additional B-site configuration entropy term for $SrCo_{0.25}Fe_{0.75}O_3$, which corresponds to -0.04 eV per formula unit and will further stabilize the $SrCo_{0.25}Fe_{0.75}O_3$, is neglected in both Fig. 9 (a) and (b).